Modelling and analysis of a bladed drum subject to the Coriolis and mistuning effects

Anthony Tacher, Fabrice Thouverez, Jason Armand

Version of Record: https://www.sciencedirect.com/science/article/pii/S0020740321006986
Manuscript_f7ea9ce5c815690b14520fcc3be2fd1c

Modelling and analysis of a bladed drum subject to the Coriolis and mistuning effects

Anthony Tacher[a,b,*], Fabrice Thouverez[a], Jason Armand[b]

[a] *École Centrale de Lyon, Laboratoire de Tribologie et Dynamique des Systèmes, UMR CNRS 5513, 36 avenue Guy de Collongue, Écully, 69134, France*
[b] *Safran Tech, Digital Sciences & Technologies, Rue des Jeunes Bois, Châteaufort, Magny-Les-Hameaux, 78114, France*

Abstract

The interaction between the Coriolis and mistuning effects on a finite-element model (FEM) of a simplified bladed drum compressor has been investigated in this paper. The Subset of Nominal Modes (SNM), the Component Mode Mistuning (CMM) and the Integral Mode Mistuning (IMM) techniques have been chosen and adapted to consider the reduction of the Coriolis matrix. Both free and forced responses of the ROMs have been validated using the FEM solutions as the benchmark. A new analysis using Monte Carlo simulations has been performed to consider disc and blade mistuning independently, and to study the domination of one over the other. The impact of the Coriolis effect has been highlighted through observation of the model with and without the Coriolis matrix. The evolution of the global dynamic behaviour with rotational speed has been investigated for the first time for different excitation frequencies and engine orders (EO). This in-depth investigation of a blisk allowed a better understanding of the interaction between the Coriolis and mistuning effects. The blade-dominated responses and the modes which remain close to the veering regions have strong mistuning effects, with significant localisation and amplitude magnification. The results mainly highlight that the disc-dominated and the blade-disc responses tend towards a tuned behaviour with the appearance of travelling waves.

Keywords: Bladed drum, Mistuning, Coriolis effect, Cyclic symmetry, Reduced-Order Model, Rotational speed

1. Introduction

Civil aircraft engines are complex structures for which it is very important to control vibration amplitudes for certification and service life expectancy. Finite-element models (FEM) of structures are built to understand and quantify the dynamic behaviour of bladed discs under operating conditions. These models are also used to reduce the need for costly life-size tests. The aim of reduced-order models (ROMs) is to minimise the computational cost of industrial models, which typically involve millions of degrees of freedom while retaining high accuracy. Bladed discs are divided into N equal sectors to reduce the modelling size and computational cost by using the FEM of one reference sector [1]. This property, known as cyclic symmetry, cannot be obtained perfectly in real structures because of deviations between sectors which result from manufacturing tolerances and the natural wear properties of materials. This physical phenomenon, called mistuning, leads to the occurrence of a standing wave with the localisation of vibrations on one or more blades and a maximum amplitude response larger than those predicted in the tuned model [2, 3, 4].

The Coriolis effect is usually considered as being negligible in the vibration analysis of bladed discs because it does not significantly change the natural frequencies or the forced response behaviour [5]. However, it has recently been shown that the Coriolis effect can lead to significant changes in the dynamic properties of bladed discs exhibiting a strongly coupled motion between the disc and the blades [6, 7]. A bladed drum with a relatively flexible disc may therefore exhibit a significant Coriolis effect [8, 9, 10]. In periodic structures,

*Corresponding author
Email addresses: anthony.tacher@ec-lyon.fr (Anthony Tacher), fabrice.thouverez@ec-lyon.fr (Fabrice Thouverez), jason.armand@safrangroup.com (Jason Armand)

the Coriolis effect splits the natural frequencies of the twin modes in a forward travelling wave (FW) mode which propagates in the same direction as that of the rotational speed, and a backward travelling wave (BW) mode which propagates in the opposite direction [11].

The analysis of a mistuned bladed drum implies the need to model the full structure with all the sectors, which can significantly increase the computational cost. It is possible to avoid this by using general linear reduction methods such as that of Craig-Bampton [12], or more specific ROMs that have been developed for linear mistuned bladed discs and that will be mentioned later in this article [13]. Some of them have been developed with the inclusion of the Coriolis matrix, but the numerical validations have generally been made without taking it into account. In some publications, ROMs have been created with the consideration of the Coriolis effect. Waldherr and Vogt [14] used an extension of the SNM to take the Coriolis effect into consideration. Wang et al. [15] performed a similar reduction with the CMM. Yan et al. also used the SNM to reduce the Coriolis matrix [16] and developed a nonlinear ROM for a model with nonlinear coating in order to take the Coriolis effect into account. Zhang et al. [17, 18] used the Craig-Bampton method to reduce and analyse a mistuned bladed disc considering the Coriolis effect, but no numerical validation against the non-reduced FEM was outlined in the paper. The primary focus of this paper is to adapt different existing reduced-order modelling methods for mistuned blisks to consider the Coriolis effect and to compare the accuracy and efficiency of the different methods. The study is focused on the SNM [19], the CMM [20] and the IMM [21], the results of which are compared to those obtained on a reference mistuned model for validation. These methods have been chosen for their simplicity of implementation, robustness, popularity in the literature and adaptability to the Coriolis matrix. The considered model is a FEM representative of a simplified industrial low pressure compressor bladed drum presenting a strong Coriolis effect and in which mistuning is randomly distributed among the blades.

Some research has shown that the Coriolis effect strengthens the mistuning effect. Huang and Kuang [22] used an analytical model to conclude that the Coriolis effect contributes to enhancing the localisation phenomenon because of the mistuning. Nikolic et al. [6] used a lumped mass model to find that the Coriolis effect can increase the maximum response level of a blade in a mistuned bladed disc. Conversely, some research has shown that the Coriolis effect mitigates the mistuning effect. Almeida et al. [23] experimentally observed the evolution of modes from a standing wave at rest to a travelling wave at high speed using a mistuned centrifugal compressor. Ruffini et al. [24] made the same experimental observation with a simplified blisk designed to exhibit a strong Coriolis effect. Lastly, some research has shown mixed results on the interaction. Xin and Wang [25] studied the modes of a FEM of a realistic compressor bladed disc and concluded that depending on the mode, the Coriolis effect can increase or reduce the mode localisation phenomenon. Kan and Xu [26] reported the same conclusions on the forced response localisation of a similar FEM compressor. Kan et al. [27, 28] studied the amplitude magnification of the forced response and, as for localisation, found that the Coriolis effect can increase or decrease the maximum amplitudes.

All these contributions show the need to take the Coriolis effect into account during the design stage of mistuned bladed discs with prominent radial flexibility. However, the coexistence of the Coriolis and mistuning effects and the dominance of one over the other are not yet fully understood. A study with a lumped mass model was investigated in [29]. Some modes become isolated in frequency because of the frequency split due to the Coriolis effect. Therefore, the behaviour of the isolated in frequency mistuned modes is close to the behaviour of the tuned modes with increasing rotational speed. However, when the modes are in veering regions or high modal density regions, the mistuning effect is predominant, even if it is at a high rotational speed. Mistuning is a random quantity and the study of only one mistuning pattern is not sufficient to fully understand the interaction between the Coriolis and mistuning effects. The application of Monte Carlo simulations is needed to predict the global behaviour of the mistuned system [30, 31, 32].

The main objective of this paper is to analyse the interaction between the Coriolis and mistuning effects on a reduced-order model of a bladed drum using Monte Carlo simulations, which allows an estimation of the global behaviour of the system for different rotational speeds and mistuning levels. The analyses are focused on three different regions. The first region presents only one disc-dominated mode and a strong Coriolis effect. The second region presents a high density of blade-dominated modes with different nodal diameter numbers. The last region is a veering region where the maximum sensitivity to mistuning is known to arise [33].

The paper is summarised as follows. The three selected reduction techniques accounting for the inclusion of the Coriolis and mistuning effects are summarised in section 2. The studied FEM is introduced in section

3 and the ROMs are validated in terms of free and forced responses. For the free response, the mode shapes with and without Coriolis are compared. Section 4 starts with the description of the Monte Carlo simulation and its accelerated version using Weibull distribution [34]. Then the localisation of the mistuning on the model is investigated to show the best reduction method to use for this model. Next, a focus on the behaviours with and without the Coriolis effect is provided. Finally, the evolution of mistuning with rotational speed in three different regions is analysed.

2. Reduction techniques for the Coriolis and mistuning effects

Among all the ROMs that have been developed for linear mistuned bladed discs, one can mention the Secondary Modal Analysis Reduction Technique (SMART) proposed by Bladh et al. [35, 36], which used the Craig-Bampton method and condensed the interface degrees of freedom (dofs) using cyclic symmetric properties. Petrov et al. [37] developed a method in which the mistuning is introduced by lumped masses, dampers and springs attached to some degrees of freedom of the blades. Yang and Griffin [38, 19] presented the Component Mode Based (CMB) and the Subset of Nominal Modes (SNM) which uses a subset of the tuned mode shapes to represent the mistuned mode shape. Feiner and Griffin [39] suggested a simplification of the SNM with the Fundamental Mistuning Model (FMM) for an isolated family, and Martel et al. [40] provided the Asymptotic Mistuning Model (AMM) which selects only the active modes of a family. Lim et al. [20] proposed the Component Mode Mistuning (CMM), which draws on the SNM and Craig-Bampton principles and is used to quickly generate a mistuned ROM. Vargiu et al. [21] extended the CMM method with the Integral Mode Mistuning to allow for mistuning on the entire sector and not only on the blade. Fitzner et al. [41] suggested the Nodal Energy Weighted Transformation (NEWT), which is a method derived from the CMM and which differs from it by the mistuning projection approach. This section presents the SNM, CMM and IMM methods for a mistuned bladed disc system.

The equation of motion of a system rotating at a constant speed is :

$$\mathbf{M}\ddot{\mathbf{q}} + (\mathbf{C} + \mathbf{G})\dot{\mathbf{q}} + \mathbf{K}\mathbf{q} = \mathbf{f}_{\text{ext}} \tag{1}$$

where $\mathbf{M}$, $\mathbf{C}$, $\mathbf{G}$ and $\mathbf{K}$ are respectively the mass, damping, Coriolis and global stiffness matrices, which is defined as follows:

$$\mathbf{K} = \mathbf{K}_{\text{l}} + \mathbf{K}_{\text{s}} + \mathbf{K}_{\text{g}}(\mathbf{q}_{\text{st}}) \tag{2}$$

The global stiffness includes the stiffness matrix $\mathbf{K}_{\text{l}}$, the softening matrix $\mathbf{K}_{\text{s}}$, and the nonlinear tangent stiffness matrix $\mathbf{K}_{\text{g}}$, estimated around a static position ($\mathbf{q}_{\text{st}}$), that results from the inertia forces and geometric nonlinearities [42]. $\mathbf{q}$ is the vector of unknown displacements around the static position. $\mathbf{f}_{\text{ext}}$ are the external forces acting on the bladed disc. The static position is found by solving a nonlinear static equation with the nonlinear vectors A.7 and A.8 and the Newton-Raphson method [43]. Each of these matrices has been constructed in the rotating frame and their expressions have been detailed in Appendix A.

2.1. Subset of Nominal system Modes (SNM)

One of the first methods developed for the reduction of small mistuned bladed disc models was the Subset of Nominal system Modes (SNM) established by Yang and Griffin [19]. With this method, the mistuning can be introduced as a perturbation in mass, stiffness, or both, independently for each degree of freedom of the full model. For the simplicity of the future developments in this article and because in general the modelling of a small mistuning is focused on the stiffness matrix, let us consider the case of stiffness mistuning only:

$$\mathbf{K} = \mathbf{K}^0 + \Delta\mathbf{K} \tag{3}$$

$\mathbf{K}^0$ is the stiffness matrix of the tuned model and $\Delta\mathbf{K}$ is the stiffness perturbation. This last matrix is often computed as a variation of Young's modulus in different parts of the model. For the mass, damping, and Coriolis matrices, they are the same for the tuned and mistuned models.

The SNM method is based on the assumption that the unknown displacement vector for a small mistuned model can be approximated as a subset of the tuned modes. Therefore, the equation of motion of the mistuned system Eq. (1) can be reduced on a subset of nominal modes composed of the tuned modes located in a

frequency range of interest and by premultiplying Eq. (1) by $\Phi^{0^{\mathsf{H}}}$ the Hermitian of Φ^0 which are the chosen eigenvectors and satisfy the system (B.4):

$$\ddot{\mathbf{p}} + (\hat{\mathbf{C}} + \hat{\mathbf{G}})\dot{\mathbf{p}} + (\Lambda^0 + \Phi^{0^{\mathsf{H}}}\Delta\mathbf{K}\Phi^0)\mathbf{p} = \hat{\mathbf{f}}_{\text{ext}} \tag{4}$$

in which the expressions of the reduced matrices can be found in Appendix B.1.

The advantages of this method are that the blades and the disc are treated as a single structure, the tuned mode can be calculated using the cyclic symmetry properties to accelerate the computing time of the reduction basis and the reduced model has as many degrees of freedom as the number of retained modes. Furthermore, there is no need to calculate the reduced tuned mass and stiffness matrices as they simply are the identity and diagonal eigenvalues matrices. The weak point of this method is the calculation of the reduced perturbation matrix, because it is a matrix operation of the same size as the full model which can be very time-consuming for a Monte Carlo simulation.

2.2. Component Mode Mistuning (CMM)

The Component Mode Mistuning method (CMM) was first proposed by Lim and al. [20]. In this method, the system is divided into different substructures. The first substructure is the whole tuned bladed disc, for which the ROM is generated using the tuned modes as in the SNM method. The other substructures are the blade mistuning components defined by the difference between the mistuned blades and the tuned blades. The mistuning can be introduced in mass or stiffness, but as for the SNM, the development here will be focused on the stiffness mistuning only. However, in this method, the mistuning can only be considered for the blades as represented in Fig. (1a).

(a) (b)

Figure 1: Two different patterns to introduce mistuning in bladed disc models where the different colors represent the deviations between sectors. In Fig. (a), the mistuning is applied on the blade and in Fig. (b) the mistuning is on all the sector.

For small mistuning, the CMM and SNM are very similar in the reduced equation of motion. The difference stems from the mistuning projection, introduced by Bladh et al. [44]. By assuming that the mode shapes of the tuned and mistuned blades are the same, the mistuned matrix is projected onto the chosen eigenvectors Φ_{CB} of the cantilevered tuned blade fixed at the blade-disc interface. However, these modes are not sufficient to describe the displacements at the blade-disc interface. If these displacements are not small, it is necessary to introduce constraint modes Ψ_{CB}, whose expression is given in (B.11).

In many articles referring to the CMM, there is an assumption that the displacements at the blade-disc interface are very small, so that only the dominant cantilevered blade modes are sufficient to project the mistuning. In the case of a bladed disc model with a strong Coriolis effect, the interaction between the blades and the disc is very strong and the displacements at the blade-disc interface are not negligible, so they will be accounted for in the present article. In order to be able to compare the CMM and SNM methods with a full model, a proportional mistuning will be considered, as follows:

$$\Delta\mathbf{K}_n^{\text{b}} = \delta_n \mathbf{K}^{\text{b}} \tag{5}$$

where superscript b illustrates the tuned blade and subscript n indicates the n^{th} sector.

With all these assumptions, the expression $\Phi^{0\mathsf{H}}\Delta\mathbf{K}\Phi^0$ of Eq. (4) becomes:

$$\Phi^{0\mathsf{H}}\Delta\mathbf{K}\Phi^0 \approx \sum_{n=1}^{N} \delta_n \mathbf{Q}_n{}^{\mathsf{H}}\mathbf{T}_{\mathrm{CB}}{}^{\mathsf{H}}\mathbf{K}^{\mathrm{b}}\mathbf{T}_{\mathrm{CB}}\mathbf{Q}_n \tag{6}$$

where $\mathbf{T}_{\mathrm{CB}}$ is the Craig-Bampton transformation matrix and $\mathbf{Q}_n$ the modal participation factors matrix. More details about their expressions and the calculation methods are given in Appendix B.2.

One advantage of this method compared to the SNM is that the mistuning parameters δ_n are expressed directly in the reduced space, and the expression $\left(\mathbf{Q}_n{}^{\mathsf{H}}\mathbf{T}_{\mathrm{CB}}{}^{\mathsf{H}}\mathbf{K}^{\mathrm{b}}\mathbf{T}_{\mathrm{CB}}\mathbf{Q}_n\right)$ has to be calculated only once for each tuned sector and a given subset of nominal system modes. This allows fast generation of ROMs with different mistuning patterns without going back to the full model, and it is really useful for Monte Carlo simulations.

2.3. Integral Mode Mistuning (IMM)

The Integral Mode Mistuning proposed by Vargui and al. [21] is an extension of the CMM to take into account sector mistuning instead of blade mistuning, as shown in Fig. 1b. As for the SNM and CMM, the IMM uses the small mistuning approximation to write Eq. (4). The mistuning matrix is no longer projected onto the cantilevered blade modes. They are replaced by the modes of an entire tuned sector with free interfaces. Then, the tuned modes Φ_n^{s} are expressed as a linear combination of the free-interface sector modes Φ^{FS} using participation factors $\mathbf{Q}_n$. Its expression is given in Appendix B.3.

Thanks to the IMM, the expression $\Phi^{0\mathsf{H}}\Delta\mathbf{K}\Phi^0$ of Eq. (4) becomes:

$$\Phi^{0\mathsf{H}}\Delta\mathbf{K}\Phi^0 \approx \sum_{n=1}^{N} \delta_n \mathbf{Q}_n{}^{\mathsf{H}}\Lambda^{FS}\mathbf{Q}_n \tag{7}$$

The advantages of the IMM are the same as those of the CMM: the mistuning parameters δ_n are expressed directly in the reduced space, and the expressions $\mathbf{Q}_n{}^{\mathsf{H}}\Lambda^{FS}\mathbf{Q}_n$ have to be calculated only once. However, with the full CMM developed here, there is a need to calculate constraint modes, which is not the case for the IMM. In contrast, the cantilevered blade mode shapes are well suited to the mode shapes of the whole tuned structure, which is not necessarily the case of the free-interface modes, since the free interface allows more flexibility on the disc than in the whole structure. As a consequence, the IMM requires more free-interface modes than the CMM requires cantilevered blade modes.

3. Reduced-Order Model validation

Now that the different reduction methods have been presented, it is necessary to validate them for the numerical model used in the analysis of the interaction between the Coriolis effect and mistuning. First the numerical model will be presented, then the validation will be done for three different reduction methods, firstly in the case of free response and then in the case of a forced response.

3.1. Model description

The model chosen to study the interaction between the Coriolis effect and mistuning is a simplified industrial bladed drum of a low-pressure compressor, with only one row of blades and 20 sectors. This model presents a high sensitivity to the Coriolis effect over some modes because the drum flexibility and allows a strong radial displacement of the rotor coupled with a tangential displacement [10]. To conduct a comprehensive study of the interaction between the Coriolis and mistuning effects, a wide range of rotational speeds is considered, and 10,000 rpm corresponds to the maximal speed of this study at which the Coriolis effect is the strongest. For this reason, the numerical simulations for the validation were done at 10,000 rpm.

The full FEM is presented in Fig. 2a and was set as the benchmark for the comparison with the ROM. It is discretised using 33,140 quadratic elements with 107,520 nodes. The drum is clamped on the 3,200 backside nodes, represented by a blue surface in Fig. 2b, which gives a full-size model of 312,960 dofs. As mentioned before, the calculation of the tuned eigenvectors and eigenvalues can be done using the cyclic

Table 1: Material properties of the standard steel.

Material property	Value	Unit
Mass density (ρ)	7850	kg/m^3
Young's modulus (E)	200	GPa
Poisson's ratio (ν)	0.3	-

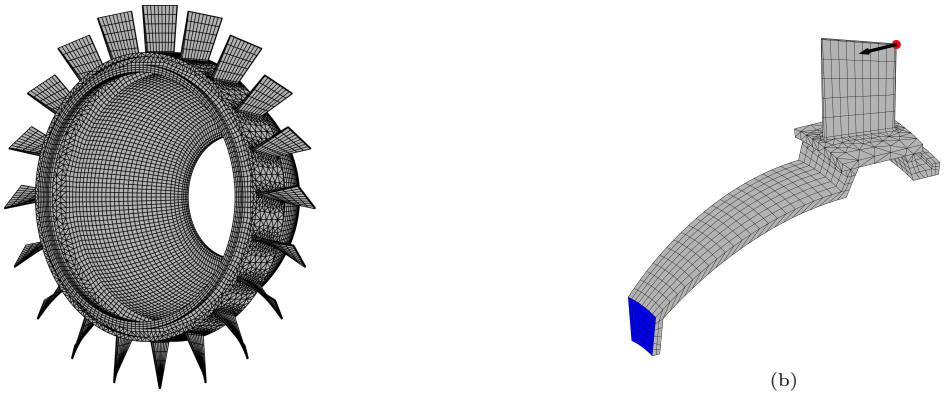

(a) (b)

Figure 2: Finite element mesh for the 20-sector bladed drum. (a) Representation of the full assembly model and (b) representation of only one sector with the clamped nodes localised on the blue surface [■]. The excitation is applied to a node at the tip of the blade represented by a red point [●] and the excitation vector is directed along the axis of rotation represented by a black arrow. [➡].

symmetry and modelling only one reference sector of 15,648 dofs (Fig. 2b) [1, 11]. The material used for the modelling is a standard steel of which the properties are listed in Table 1.

The evolution of the modes with the rotational speed can be summarised in a Campbell diagram (Fig. 3). That represents their frequency versus their nodal diameter number. The backward travelling wave (BW) modes are represented by dashed lines while the forward travelling wave (FW) modes are represented by solid lines. It can be observed that some modes are split in frequency between their FW and BW modes as the rotational speed increases due to the Coriolis effect [45], especially for the 1ND and 2ND modes of the first family and the 3ND of the second family. All of these modes are disc-dominated modes except for the 1ND-BW mode of the first family, which is a blade-disc mode. The accumulation of modes above the 1ND-BW 1 are blade-dominated modes with a first flexural mode and different nodal diameter numbers.

The modes of a tuned structure at a given rotational speed are shown in Fig. 4a, representing their frequency versus their nodal diameter number. Disc-dominated modes are represented by slanted lines; by contrast, the horizontal lines represent blade-dominated modes. Around 700 Hz, it is dominated by the first flexural mode (1F) (Fig. 5a), around 2,000 Hz, it is the first torsional mode (1T) (Fig. 5b), and around 2,500 Hz, it is the second flexural mode (2F) (Fig. 5c). At the crossing between two modal families, there is what appears to be a veering region : the blade and disc-dominated modes veer away from each other, and the modes in this region are a combination of blade and disc motions. Three of these regions are surrounded by squares in Fig. 4a. Only the veering for the 1ND between the first and the second families will be studied later on in this article due to the proximity of the modes as shown in Fig. 4b. It is known that localisation due to mistuning can be strong in these regions [46, 33, 34].

The force response study will be focused on three different regions and EOs, which are surrounded by circles in Fig. 4a. These regions will be named from left to right: the veering region, the low modal density region and the high modal density region. The characteristics of each region will be developed later in the article.

3.2. Free response

This subsection is devoted to validating the SNM, CMM and IMM ROMs for a free response. The numerical simulations investigating the interaction between the Coriolis effect and the mistuning will be in

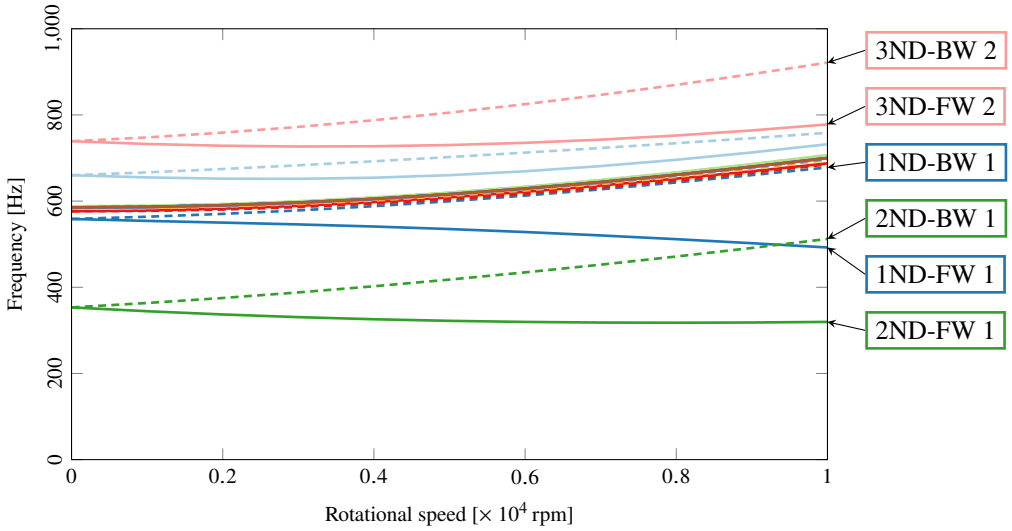

Figure 3: Campbell diagram of the 24 first modes of the bladed drum between 0 rpm and 10,000 rpm. All different nodal diameter modes (ND) are represented with different colours. The solid curves represent the forward wave modes (FW) [—] and the dashed curves represent the backward wave modes (BW) [- -]. The modes with a significant frequency split due to the Coriolis effect are tagged in the figure. The number after FW or BW characterises the modal family number.

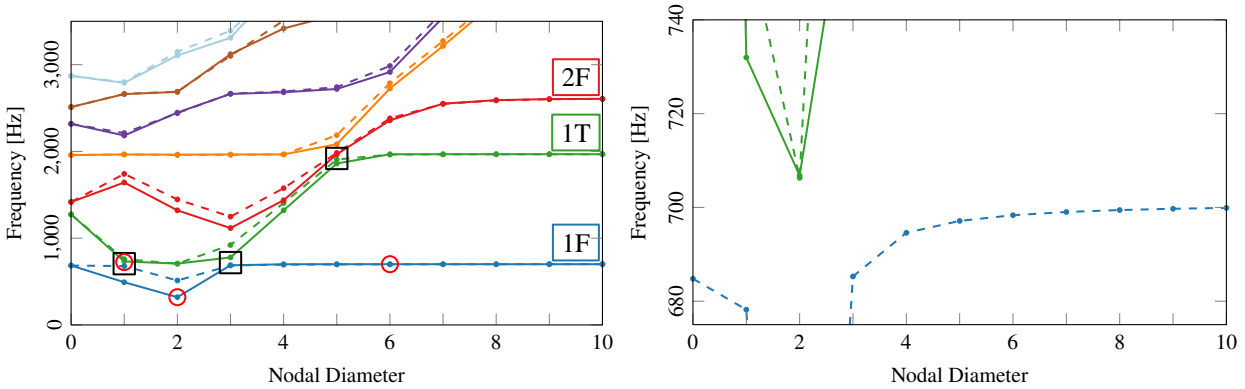

Figure 4: Natural frequencies versus number of nodal diameters for the tuned rotor for the 14 first modes at 10,000 rpm. All different modal families are represented with different colours. The solid curves represent the forward wave modes [—] and the dashed curves represent the backward wave modes [- -]. Around 700 Hz, the mode shape is dominated by the first flexural mode (1F) , around 2,000 Hz, it is the first torsional mode (1T), and around 2,500 Hz, it is the second flexural mode (2F). The veering regions are shown by black squares [□] and the studied regions for the numerical simulations are localised by red circles [○]. (a) Overall view. (b) Frequency expansion on the veering region.

the frequencies around the first family modes and some modes of the second family. For this reason, the validation will focus on the modes below 1,000 Hz for each method, which correspond to the 26 first mistuned modes. As mentioned in the previous section, the mistuning is introduced by a mistuning parameter δ_n for each sector or blade depending on whether the mistuning is introduced on the whole sector or only on the blade Eq. (5). The mistuning parameters for the validation simulations are generated using a normal distribution with zero mean and 2.5 % standard deviation. The mistuning pattern is summarised in Table 2.

3.2.1. Mode choice of the reduction basis

In the previous section, the tuned eigenvectors were determined from the system in Eq. (B.4), which did not take into account the Coriolis matrix. With the Coriolis matrix, the system has to be passed in the state-space representation, which doubles the size of the problem and increases the computational time.

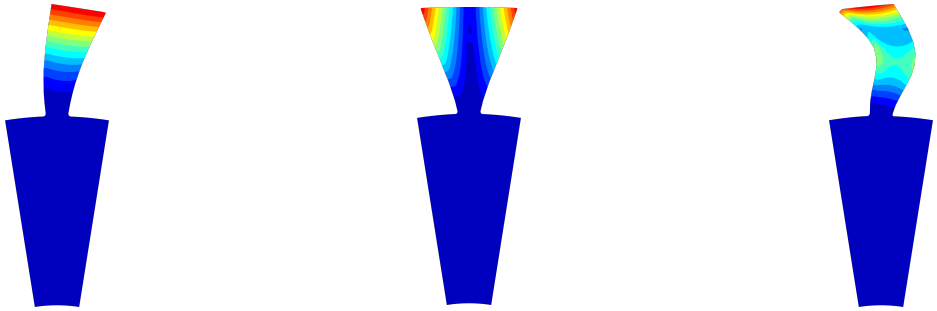

(a) (b) (c)

Figure 5: Mode shapes of the three first blade-dominated mode families. (a) First flexural mode around 700 Hz. (b) First torsional mode around 2,000 Hz. (c) Second flexural mode around 2,500 Hz.

Table 2: Mistuning pattern introduced in the FEM using a normal distribution with zero mean and 2.5 % standard deviation.

Sector	1	2	3	4	5	6	7	8	9
δ_n	-0.00256	-0.00604	0.00798	0.00782	-0.02162	-0.00075	-0.00412	0.01569	0.02733
Sector	10	11	12	13	14	15	16	17	18
δ_n	0.02773	-0.02159	0.00193	-0.03035	-0.02784	-0.00017	0.03832	-0.01924	0.00928
Sector	19	20							
δ_n	-0.00564	0.02793							

The tuned eigenvectors calculated with and without the Coriolis matrix have been compared using the Normalized Cross Orthogonality check (NCO) [47]. This is very similar to the Modal Assurance Criterion (MAC) but it also gives information about the orthogonality of the modes with regard to a matrix.

$$NCO(i,j) = \frac{|{\phi_i}^{\mathsf{H}} \mathbf{B} \tilde{\phi}_j|^2}{|{\phi_i}^{\mathsf{H}} \mathbf{B} \phi_j||\tilde{\phi}_i^{\mathsf{H}} \mathbf{B} \tilde{\phi}_j|} \tag{8}$$

where Φ_i is the mistuned mode of the FEM and $\tilde{\phi}_j$ is the mistuned mode of the ROM projected onto the FEM dofs using the subset of nominal mode basis. $\mathbf{B}$ is the augmented mass matrix originating from the state-space representation of the full model [48]. The state-space representation, imposed by the Coriolis matrix, also applies to the modes ϕ_i and $\tilde{\phi}_j$.

$$\mathbf{B} = \begin{bmatrix} \mathbf{K} & \mathbf{0} \\ \mathbf{0} & \mathbf{M} \end{bmatrix} \tag{9}$$

If the NCO has a value near one, it indicates that the eigenvectors are very similar; on the contrary, a NCO near zero means that the eigenvectors are almost orthogonal with respect to the matrix $\mathbf{B}$. For the sake of clarity, Fig. 6 shows the NCO matrix for the eigenvectors of the two first tuned families, but the results are similar for the other families. ϕ_j are the modes calculated without the Coriolis matrix, and ψ_i the modes calculated with the Coriolis matrix. There is an excellent accuracy between the modes calculated with and without the Coriolis matrix. On the diagonal, only five NCO indexes are below 0.95 -surrounded by squares in Fig. 6- and four indexes are above 0.05 NCO for the off-diagonal terms which are surrounded by circles in Fig. 6. These indexes correspond to the 1ND-BW and 3ND-FW modes of the first and second families and the 5ND-BW of the second family. All of these modes are in veering regions, as evidenced by Fig. 4a. This can be explained by the fact that because of the Coriolis matrix, the modes of two families near a veering region will be more or less close to each other in frequency and the shapes of the tuned modes evolve with the location in the veering region. For example, 1ND-BW modes of the first and second families are separated by a delta of 138.67 Hz without the Coriolis matrix, while with the Coriolis matrix, this delta is reduced to 80.27 Hz (Fig. 4b). 1ND-FW and 1ND-BW modes of the first family have the same shape without Coriolis, but with Coriolis, 1ND-FW mode evolves to a disc-dominated mode and 1ND-BW to a blade-dominated mode.

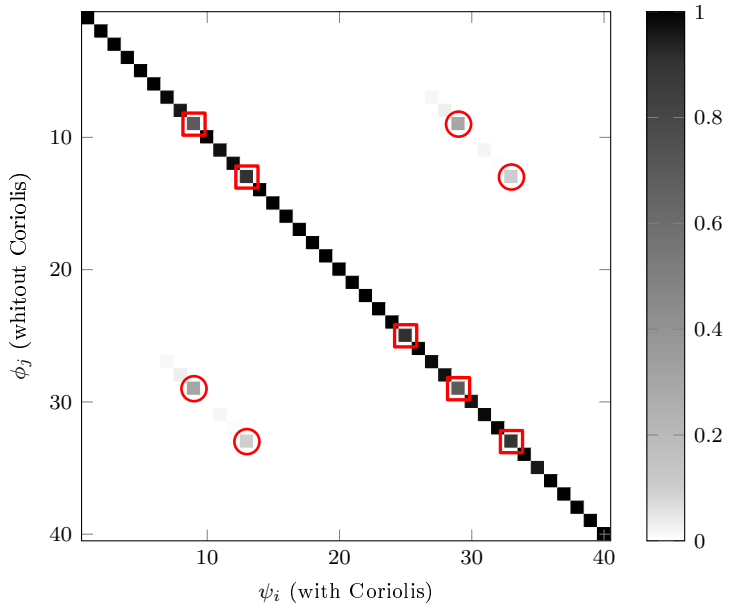

Figure 6: Matrix of the Normalized Cross Orthogonality check (NCO) for the comparison between the eigenvectors calculated with Coriolis (ψ_i) and the eigenvectors calculated without Coriolis (ϕ_j) at 10,000 rpm. [○] NCO>0.05 for the off-diagonal terms. [□] NCO<0.95 for the terms on the diagonal. A value near one indicates that the eigenvectors are very similar and a value near zero means that the eigenvectors are almost orthogonal with respect to the augmented mass matrix **B** (Fig. (9)).

One of the hypotheses is that the shape of a tuned mode with the Coriolis effect in a veering region can be captured well by using a combination of tuned modes without considering the Coriolis effect. Therefore, it is possible to construct the basis without the Coriolis matrix but still be able to capture the Coriolis effect. For this reason, all the reductions carried-out hereafter in this article, are constructed without taking the Coriolis matrix into account, but the reduced Coriolis matrix is still calculated using Eq. (B.8).

With an equivalent mistuning pattern and the same reduction basis, the CMM ROM accuracy converges to the SNM ROM accuracy with the number of cantilevered blade modes which can be better observed by examining the modal participation factors in Eq. (B.12): if one takes all the cantilevered blade modes, the subset of nominal modes limited to the blade dofs Φ_n^{b} is the same as the one used in the SNM. The same can be done for the IMM ROM, for which the accuracy converges to the SNM ROM accuracy when increasing the number of free-interface sector modes using Eq. (B.21). The choice was made to set the SNM as a reference for the CMM and IMM so that the choices of the tuned modes are made with the SNM and then one only needs to choose the number of cantilevered modes for the CMM and the number of free-interface modes for the IMM to converge to the SNM ROM.

For this reason, there are two cases with the SNM. The first one is the introduction of a proportional stiffness mistuning on the blade equivalent to the CMM (Eq. (5)), and the second one is a proportional stiffness mistuning on the whole sector equivalent to the IMM. The tuned modes of the 25 first families' modes are selected to constitute the basis of the reduction, forming a final ROM of 500 dofs. The three first cantilevered modes are, respectively, the first flexural mode, the first torsional mode and the second flexural mode, which are also the mode shapes of the blade-dominated modes of the three first families. These cantilevered modes are chosen to calculate the modal participation factors (Eq. (B.14)) used in the CMM method and show a good convergence to the results calculated using the SNM. The first free-interface mode shapes are less accurate than the mode shapes of the whole tuned structure. It is necessary to use the 200 first free-interface modes to compute the modal participation factors (Eq. (B.22)) used in the IMM and have a good convergence to the SNM ROM results.

The computational cost to obtain each ROM is given in Table 3.

Table 3: Computational cost to perform the SNM, CMM and IMM reductions. The simulations were run on an Intel(R) Core(TM) i7-10700K CPU @ 3.80GHz.

	SNM	CMM	IMM
Tuned modes	48 s	48 s	48 s
Cantilevered blade modes	-	<1 s	-
Free-interface sector modes	-	-	4 s
Matrices computing	16 s	8 s	4 s
Total	**64 s**	**56 s**	**60 s**

3.2.2. Comparison of the eigenvalues and eigenvectors of the ROMs with the FEM

The first criterion of validation is to calculate the relative error of the ROMs' natural frequencies versus the full mistuned model.

$$\varepsilon = \frac{|f_{\mathrm{ROM}} - f_{\mathrm{FEM}}|}{f_{\mathrm{FEM}}}.100 \tag{10}$$

where f_{ROM} is the natural frequency of the mistuned ROM and f_{FEM} the natural frequency of the mistuned FEM.

The error values are all below 0.01 % for an average of around 0.007 % in the four cases. The NCO matrices show an excellent modelling of the mistuned mode shapes with a minimum NCO of 0.999 in the diagonal and a maximum of 0.001 for the off-diagonal terms, which demonstrates that the 25 first families are sufficient to estimate properly the 26 first natural frequencies and mode shapes using the SNM. Besides, the three first cantilevered modes using the CMM, and the 200 first free-interface modes using the IMM are sufficient to have a good convergence to the SNM ROM.

3.3. Forced response

Now that the ROMs have been validated for a free response, it is necessary to validate these same ROMs in forced response. The computing of the excitation force and damping matrix is explained in Appendix C.

The validation has been focused on three different cases. The first region is around 320 Hz with a 2EO-FW excitation. It corresponds to the tuned 2ND-FW mode, which exhibits a strong Coriolis effect due to the split of the frequencies between the FW and BW modes and a disc-dominated shape. The second region is around 700 Hz with a 6EO-FW excitation. It is a high modal density region of blade-dominated modes. The third region, around 678 Hz with a 1EO-BW excitation, is related to the veering region surrounded in Fig. 4a between the 1ND-BW modes of the first and second families. These simulations are effective samples to test the ROMs because all of these regions have different dynamic behaviours regarding the Coriolis and mistuning effects.

The simulations are separated into two configurations : the blade mistuning configuration with the CMM and SNM ROMs, and the sector mistuning configuration with the IMM and SNM ROMs. The FEM simulations are set as the benchmark for the ROMs simulations. The maximum forced responses for the different cases are plotted in Fig. 7 for the blade mistuning and Fig. 8 for the sector mistuning.

The first observation that can be made is the similarity of the responses between the blade mistuning configuration and the sector mistuning configuration, the only difference being the offset of the peak in Fig. 8a, which does not appear in Fig. 7a. The sum of the stiffness perturbations listed in Table 2 is negative. Therefore, the mistuning of the disc has a softening effect that can be observed on the forced response.

In the first case, there is one peak corresponding to the only mode located in this region. The mistuned response is very close to the tuned response represented by the dashed line (Fig. 7a and Fig. 8a). It is almost a perfect 2ND-FW response with all sectors vibrating with the same amplitude (Fig. 7b and Fig. 8b), which is a known phenomenon induced by a strong Coriolis effect on mistuning [24]. Even if the Coriolis matrix was not taken into account in the ROM construction bases, the Coriolis effect seems to be captured well, because all the ROM responses match perfectly with the full model responses.

The second case presents a strong mistuned behaviour due to the high modal density in this region with a lot of peaks compared to the tuned case (Fig. 7c and Fig. 8c), and different maximum amplitudes for all the sectors (Fig. 7d and Fig. 8d). Once again, the ROM results are very close to the benchmark, so the mistuning effect is well captured for the high modal density region with blade-dominated shapes.

Finally, for the third case, there are fewer peaks because it is not a high modal density although the amplification of the response against the tuned case is very strong (Fig. 7e and Fig. 8e). This phenomenon is known to occur in veering regions where there is a moderately weak blade-disc coupling which allows the possibility for the blades to exchange energy and for this energy to be located to a few blades, and the creation of a localisation response with a high amplitude for these few blades [3, 46] (Fig. 7f and Fig. 8f). These figures validate the use of the ROMs in the veering region where the Coriolis and mistuning effects coexist.

This section validates the use of the ROMs for the bladed drum model in both free and forced responses. The reduction bases can be calculated using the modes without the Coriolis effect as there are no significant changes in the mode shapes, which allows a faster computation of the ROMs. The computational cost to perform the forced responses are summarised in Table 4 which demonstrates the effectiveness of the reduction methods because the construction of the ROMs takes around one minute and the time saved on the forced responses is about several hours.

Table 4: Computational cost to perform forced responses with the FEM and the ROMs from the SNM, CMM and IMM in the three different regions. The simulations were run on an Intel(R) Core(TM) i7-10700K CPU @ 3.80GHz except for the FEM (*) which required too much memory and was thus performed on a supercomputer with 40 cores and 400Go of RAM.

	FEM*	SNM	CMM	IMM
Low modal density region	21 h	17 s	17 s	17 s
High modal density region	190 h	17 s	17 s	17 s
Veering region	96 h	17 s	17 s	17 s

4. Analyses of the Coriolis and mistuning effects

In this part, an investigation of the interaction between the Coriolis and mistuning effects is presented. Firstly, the Monte Carlo simulation principle will be explained because it was the principal tool of the analyses. Secondly, the investigation will be focused on the integration of the mistuning and the influence of its localisation on the bladed drum. Then it will be shown that the Coriolis forces may have a strong effect in the bladed drum simulations. Finally, the interaction will be investigated under different rotational speeds.

4.1. Monte Carlo simulation for forced response statistics

The Monte Carlo simulation allows an estimation of the statistics of forced response. More specifically, it can be used to determine the percentile values of the amplitude magnification factor versus the standard deviation of random mistuning, also called the mistuning level (σ) [30]. The amplitude magnification factor corresponds to the ratio between the maximum amplitude response of the mistuned and tuned cases. The principle of the simulation is to fix a standard deviation of random mistuning for the mistuning parameter with a standard normal distribution. This generates different random patterns of the mistuned bladed drum, for which a forced response is performed. For each pattern, the largest amplitude response is recorded and divided by the maximum amplitude of the tuned case to find the amplitude magnification factor. A Monte Carlo simulation requires a large number of analyses to estimate precisely the statistics of forced response, which can be computationally expensive.

Therefore, it is possible to accelerate the Monte Carlo simulation by estimating the amplitude magnification factor distribution [34]. This estimation is carried out using the cumulative distribution function of the three-parameter Weibull distribution for the largest value.

$$F(x) = e^{-((\lambda - x)/\delta)^{\gamma}} \tag{11}$$

where x is the random variable of the amplitude magnification, and δ, γ and λ are respectively the scale, shape and location parameters. To estimate these parameters, Eq. (11) has to be rearranged using the $\ln(-\ln(\cdot))$ operator

$$\ln(\lambda - x) = \frac{1}{\gamma}\ln(-\ln(F)) + \ln(\delta) \tag{12}$$

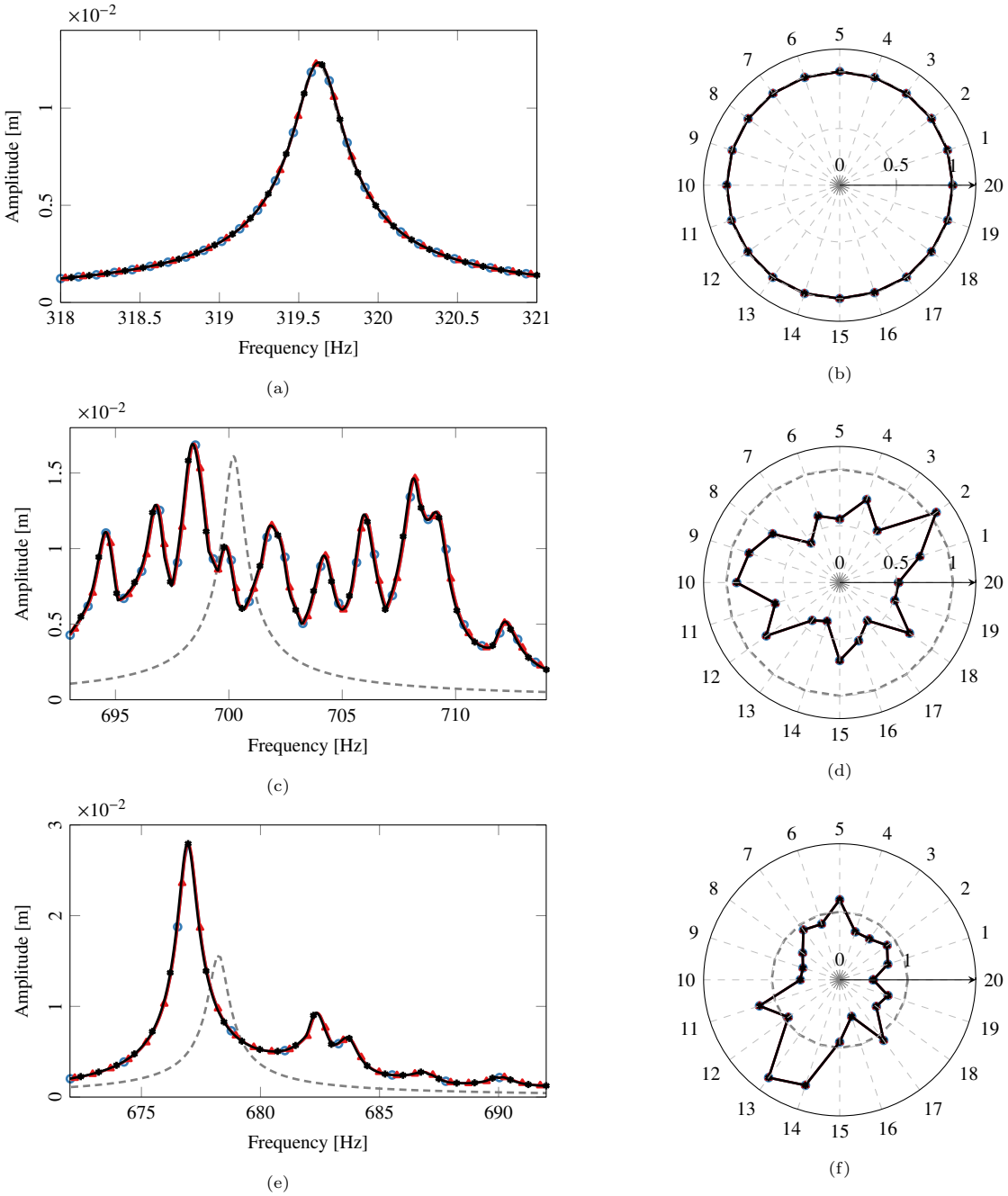

Figure 7: Maximum forced response for a blade mistuning in different frequency regions and with different excitations. [(a), (c), (e)] Maximum amplitude over the excitation frequency. [(b), (d), (f)] Maximum normalised amplitude over the blades. [(a), (b)] Low modal density region with a 2EO-FW excitation. [(c), (d)] High modal density region with a 6EO-FW excitation. [(e), (f)] Veering region with 1EO-BW excitation. The blue curves with circles [—○—] and the red curves with triangles [—▲—] represent the forced response of the ROM using respectively the SNM and CMM method. The black curves with stars [—✱—] represent the forced response of the mistuned FEM and is the benchmark for the ROM. The dashed curves in grey [- - -] represent the forced response of the tuned FEM.

The location parameter λ describes the upper limit of x. In general, the approximation of λ is given by a Whitehead approximation [49, 50]

$$\lambda = \frac{1}{2}(1 + \sqrt{N}) \tag{13}$$

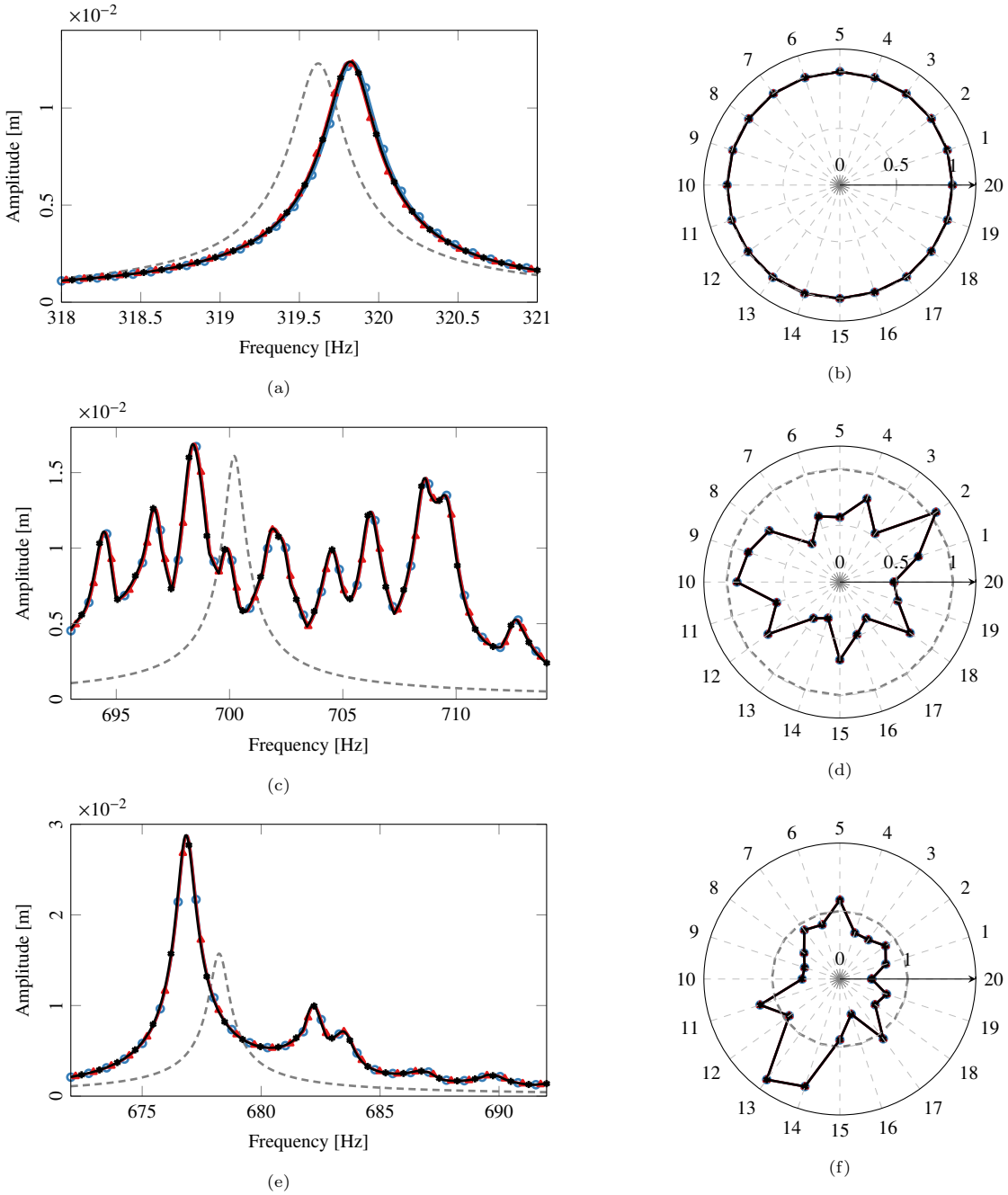

Figure 8: Maximum forced response for a sector mistuning in different frequency regions and with different excitations. [(a), (c), (e)] Maximum amplitude over the excitation frequency. [(b), (d), (f)] Maximum normalised amplitude over the blades. [(a), (b)] Low modal density region with a 2EO-FW excitation. [(c), (d)] High modal density region with a 6EO-FW excitation. [(e), (f)] Veering region with a 1EO-BW excitation. The blue curves with circles [—o—] and the red curves with triangles [—▲—] represent the forced response of the ROM using respectively the SNM and IMM method. The black curves with stars [—*—] represent the forced response of the mistuned FEM and is the benchmark for the ROM. The dashed curves in grey [- - -] represent the forced response of the tuned FEM.

This approximation works well when there is only one family of modes in the frequency range of interest, since this assumption is made by Whitehead. However, in the veering region, this limit can be exceeded by the presence of several families of modes and the results seem to be case-dependent [51, 52, 53]. For these reasons and because the maximum amplitude magnification factor is difficult to generalise for every FEM,

the value λ is assumed to be 20 % above the maximum value x given by the simulation.

By sorting the x values of the simulation and determining the associated cumulative distribution function values, the two unknowns δ and γ in Eq. (12) can be estimated using a least-squares linear regression. Finally, the amplitude magnification factor can be calculated for every value of the cumulative distribution function using the operator $e^{(\cdot)}$ in Eq. (12).

$$x = \lambda - \delta(-\ln(F))^{\frac{1}{\gamma}} \tag{14}$$

The cumulative distribution function given by the three-parameter Weibull distribution using a set of 50 mistuning patterns of the bladed drum is plotted in Fig. 9 for a 2EO-FW excitation with 2.5 % of mistuning level at 10,000 rpm. Two curves correspond to two different limit amplitude magnification factor approximations, the blue one calculated using Whitehead's formula ($\lambda = 2.736$) and the red one calculated using the 20 % above the maximum value x of the simulation ($\lambda = 1.802$). This assumption does not change the Weibull curve significantly and allows one to estimate the distribution even if the amplitude magnification factors are above Whitehead's limit.

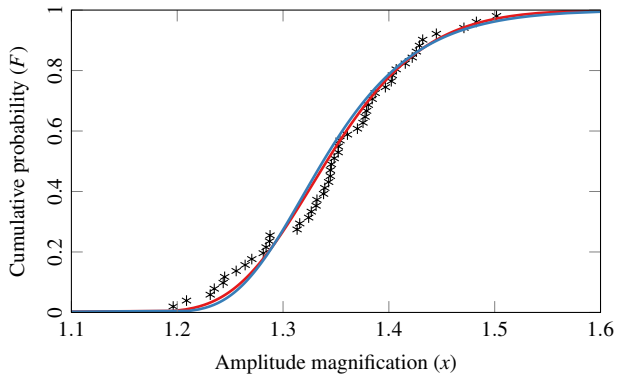

Figure 9: Two cumulative distribution functions for the accelerated Monte Carlo simulation given by the three-parameter Weibull distribution. The blue one [—] is for a location parameter $\lambda = 2.736$ and the red one [—] is for $\lambda = 1.802$. A set of 50 mistuning patterns are plotted by stars on the cumulative distribution functions from the smallest amplitude magnification value to the largest.

4.2. Influence of the mistuning locations in the bladed drum

The first investigation carried out is on the choice of the method to introduce the mistuning. As mentioned above, the mistuning can be introduced on the blades or the sectors. In most publications, the mistuning is only introduced on the blades because it is the major contributor to the amplitude magnification. However, the impact of the interface mistuning [21] or the disc mistuning [54] can have a powerful effect on the forced response when the modes have a large disc participation. As the bladed drum FEM has a significant disc participation in many of its modes, it is interesting to study the differences between a blade mistuning, a sector mistuning and a disc mistuning.

Blade, sector and disc mistuning have been investigated using the CMM, IMM, and the SNM techniques, respectively. The simulations are performed for the three different cases defined in the ROM validation section, namely the low modal density region, the high modal density region and the veering region. As the aim is to compare behaviours between different mistuning localisation cases, there is no need to plot different values of the statistical response distributions. Only the medians of the amplitude magnification factors are plotted in Fig. 10. The simulation for the low modal density region has been done at 0 rpm (Fig. 10a) and 10,000 rpm (Fig. 10b), while those for the two other regions have been performed only at 10,000 rpm.

In the low modal density region, at 0 rpm (Fig. 10a), there is an amplitude magnification due to the mistuning. The behaviours of the disc and sector mistuning are similar while the behaviour of the blade mistuning is different. At 10,000 rpm (Fig. 10b), the mistuning does not seem to have an impact on the amplitude magnification as can be observed in Fig. 7a and Fig. 8a with a maximum amplitude response very close to the tuned case, so in this case, there is no particular difference among blade, sector and disc mistuning and this will not be studied further in the investigation of the mistuning location. This different

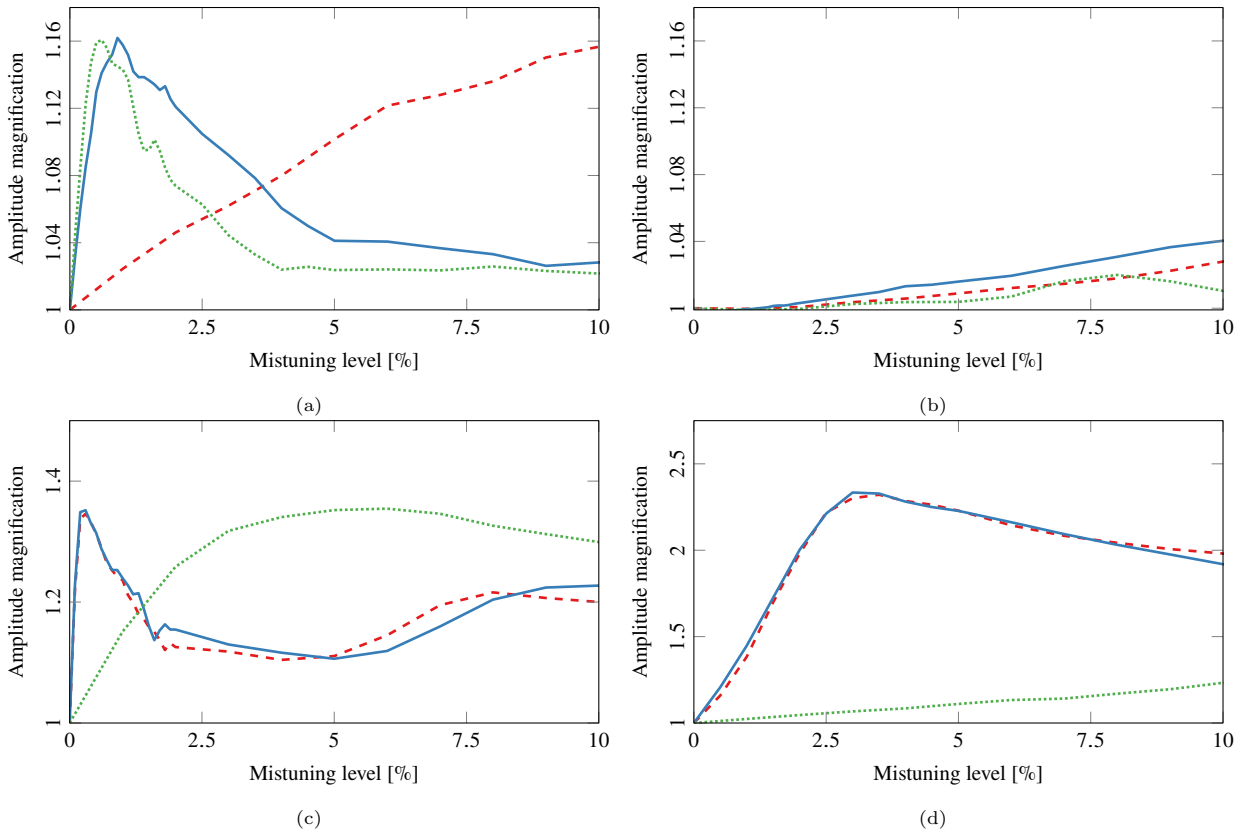

Figure 10: Comparison of the median amplitude magnification factor with the mistuning level. (a) Low modal density region with a 2EO-FW excitation at 0 rpm. (b) Low modal density region with a 2EO-FW excitation at 10,000 rpm. (c) High modal density region with a 6EO-FW excitation at 10,000 rpm. (d) Veering region with a 1EO-BW excitation at 10,000 rpm. The red dashed curves [- -], the blue solid curves [—] and the green dotted curves are respectively for the blade mistuning, sector mistuning and disc mistuning simulations.

trend between the case at 0 rpm and 10,000 rpm is mainly due to the Coriolis effect and will be further investigated and explained in the last subsection dedicated to the dynamic evolution of the system with the rotational speed. For both the high modal density region (Fig. 10c) and the veering region (Fig. 10d) at 10,000 rpm, the behaviours of the blade and sector mistuning are similar and the disc mistuning is different.

The above observations are not sufficient to determine if the mistuning effect is driven by the blade or the disc mistuning. For this reason, two additional Monte Carlo simulations were run for each region. In the first simulation, a pattern for the blade mistuning is given for a mistuning level at the local maximum of amplitude magnification, and the Monte Carlo is run for different disc mistuning levels. In the second simulation, the opposite is true: the disc mistuning pattern is given for the disc mistuning local maximum, and the Monte Carlo simulation is run for different blade mistuning levels. The mistuning level values used for the patterns are summarised in Table 5. These patterns are chosen in such a way that the mistuning amplitude magnification factors are around the median maximum values. All these simulations are run with the SNM reduction method because this method serves to separate the disc and the blade mistuning. Finally, these simulations are compared to the Monte Carlo simulations of the blade and disc mistuning alone (Fig. 11).

In the low modal density region (Fig. 11a), the fixed disc mistuning with variable blade mistuning level does not seem to be affected by the blade mistuning, as the amplitude magnification factor does not substantially change with the mistuning level. However, the amplitude magnification of the fixed blade mistuning with variable disc mistuning decreases with the mistuning level and follows the curve of the disc mistuning alone. For the high modal density region (Fig. 11b) and the veering region (Fig. 11c), the fixed blade mistuning with variable disc mistuning is not affected by the mistuning level and the disc mistuning with variable blade mistuning curves follow the blade mistuning curves.

Table 5: Mistuning level values at the local maximum of amplitude magnification for the blade and disc mistuning.

	Blade mistuning	Disc mistuning
Low modal density region	10 %	0.6 %
High modal density region	0.3 %	5 %
Veering region	3.5 %	10 %

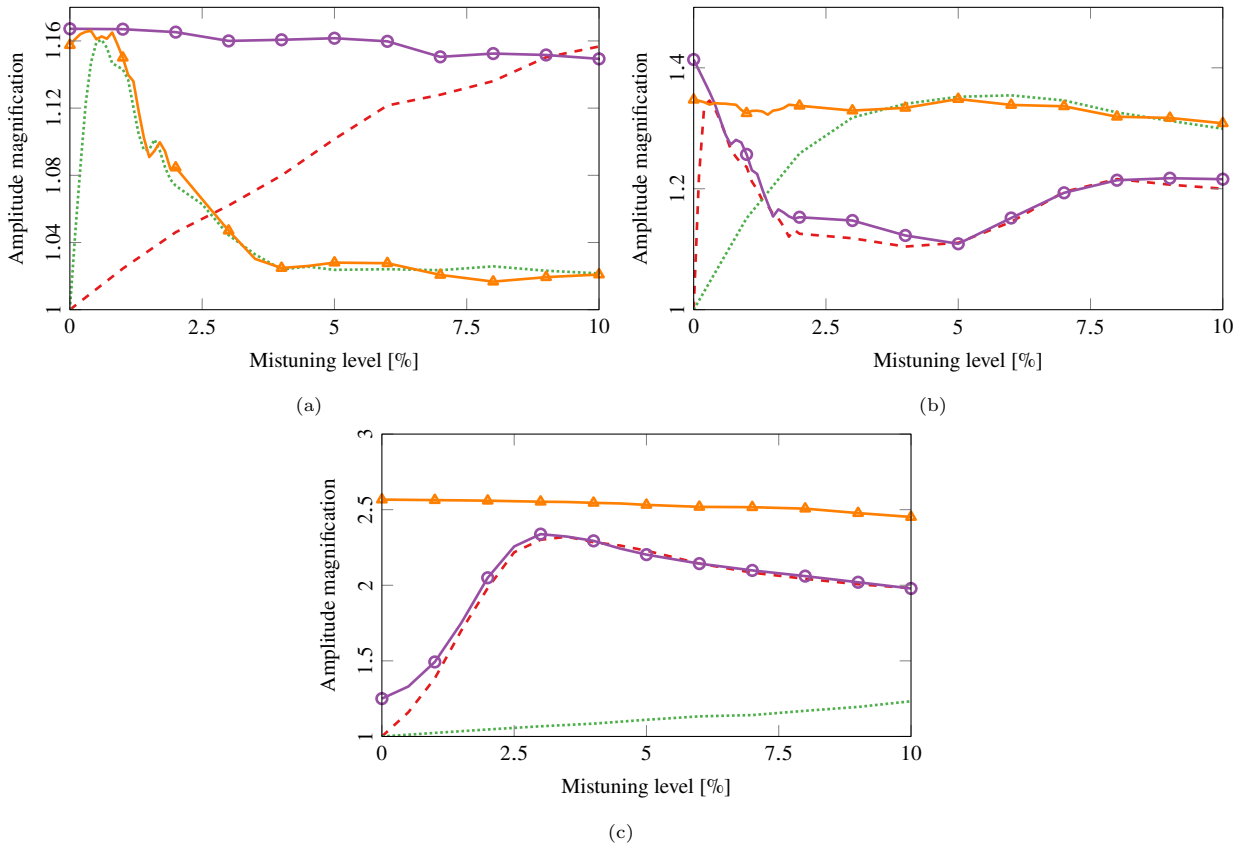

Figure 11: Comparison of the amplitude magnification factor with the mistuning level. (a) Low modal density region with a 2EO-FW excitation at 0 rpm. (b) High modal density region with a 6EO-FW excitation at 10,000 rpm. (c) Veering region with a 1EO-BW excitation at 10,000 rpm. The red dashed curves [- - -] and the green dotted curves [····] are respectively for the variable blade mistuning alone and variable disc mistuning alone simulations. The orange curves with triangles [—▲—] represent the simulations for a fixed blade mistuning with variable disc mistuning and the purple curves with circles [—○—] represent the simulations for a fixed disc mistuning with variable blade mistuning.

These simulations exhibit two distinct situations. When there is a disc-dominated mode, it is the disc mistuning that drives the mistuning effect. When it is a blade-dominated mode or blade-disc mode like in the veering region, it is the blade mistuning that drives the mistuning effect. In both cases, the sector mistuning always follows the behaviour of the predominant mistuning effect. For this reason, the simulations presented later in this article are performed with a sector mistuning using the IMM reduction method.

4.3. Coriolis requirement in the simulations

As mentioned earlier, the Coriolis effect is often neglected in bladed disc forced response. However, in the bladed drum model presently considered, the Coriolis effect is non-negligible, as can be observed with the presence of splits in the Campbell diagram of the tuned model (Fig. 3). The dynamic behaviour of a mistuned model sensitive to the Coriolis effect can change with the rotational speed [24, 29]. More recently, Zhang [17] showed that the Coriolis force cannot be ignored in the analysis of the vibration localisation

characteristics of a mistuned bladed disc FEM. For these reasons, Monte Carlo simulations with and without the Coriolis matrix were carried out at 10,000 rpm for the three different regions.

It is important to note that the simulations with and without the Coriolis matrix were not performed in the same frequency regions because the frequencies of the modes are changed by the Coriolis effect. The excitation regions for the different cases are summarised in Table 6.

Table 6: Frequency regions for the different cases with and without the Coriolis effect.

	With the Coriolis effect	Without the Coriolis effect
Low modal density region	270 Hz-370 Hz	358 Hz-458 Hz
High modal density region	650 Hz-750 Hz	650 Hz-750 Hz
Veering region	628 Hz-728 Hz	542 Hz-642 Hz

The variations in the amplitude magnification factor with the mistuning level for the different regions are plotted in Fig. 12. In the first case (Fig. 12a), the magnification is greater without the Coriolis effect due to two modes that originate from the tuned double modes near the excitation region. These two modes are split in frequency by the mistuning, and there is an interaction between them that induces an amplitude magnification. With the Coriolis effect, there is only one mode that originates from the 2ND-FW tuned mode as the 2ND-BW mode is too far because of the frequency split. Therefore, there is no interaction and no amplitude magnification.

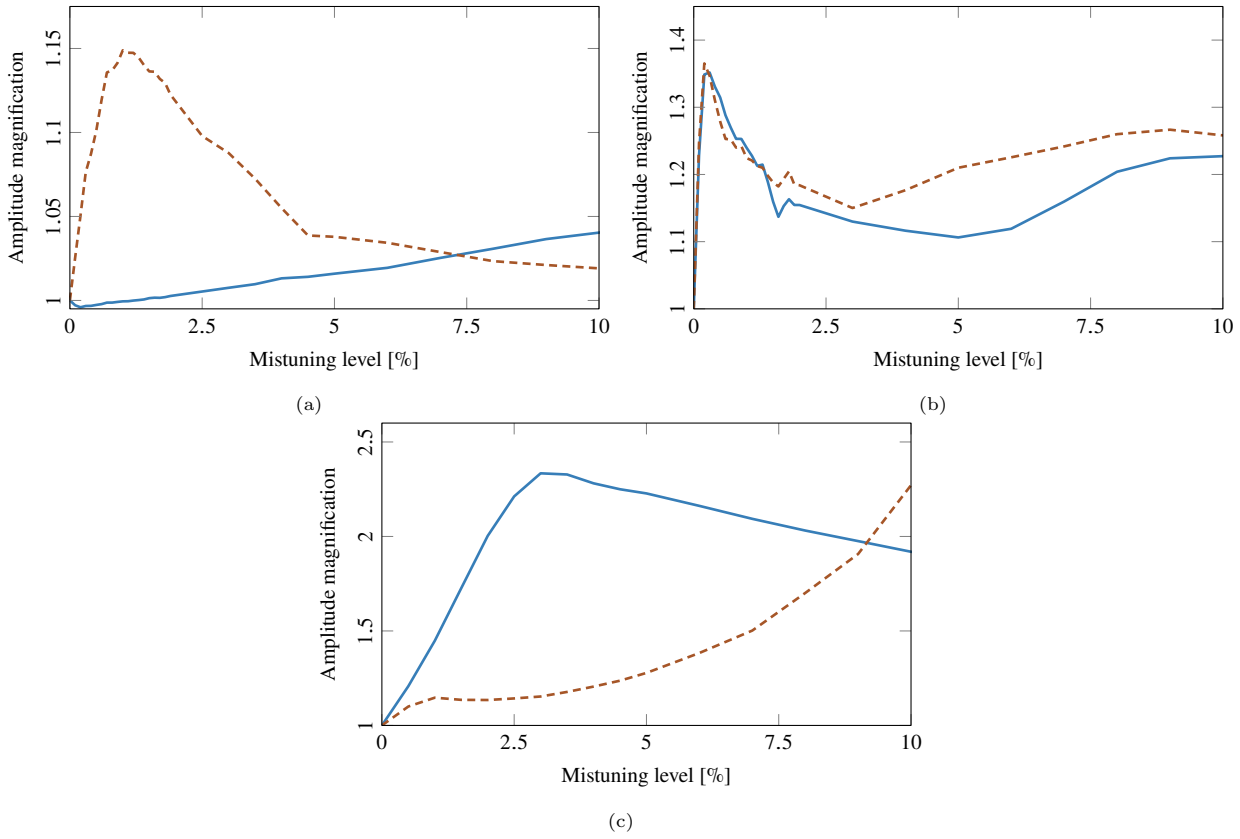

Figure 12: Variations in the amplitude magnification factor with the mistuning level at 10,000 rpm. (a) Low modal density region with a 2EO-FW excitation. (b) High modal density region with a 6EO-FW excitation. (c) Veering region with a 1EO-BW excitation. The blue curves [—] represent the simulations with the inclusion of the Coriolis effect when the brown dashed curves [- -] represent the simulations without the inclusion of the Coriolis effect.

In the second case (Fig. 12b), the Coriolis effect does not seem to have a real impact. The magnification is slightly greater, but not significantly. It can be observed in Table 6 that the region of excitation is the

same with and without Coriolis, which confirms that near blade-dominated modes, the Coriolis effect can be negligible, as reported in most of previous papers investigating mistuning.

The difference in behaviour is the most direct in the third case (Fig. 12c) and depends on the mistuning level. Below 9 %, the case with the Coriolis effect has an higher magnification factor than the case without the Coriolis effect and, above 9 %, the opposite behaviour holds. The local maximum amplitude magnification appears around 3.5 % of mistuning level with the Coriolis effect, while it does not seem to have a local maximum below 10 % for the case without Coriolis.

This quick investigation shows that it is essential to take the Coriolis effect into account when there is disc participation in the response, especially in the veering region where the behaviour can be completely different when the Coriolis effect is not taken into account.

4.4. Dynamic evolution with the rotational speed

The Coriolis effect depends on the rotational speed, which is not the case of mistuning. It is therefore expected that the interaction between the Coriolis and mistuning effects varies with the rotational speed. The forced response statistics will be investigated further under several rotational speeds in the three different regions and with the introduction of three criteria. The first criterion is the amplitude magnification induced by the mistuning. The second criterion is the average change of amplitude (ACA) given at the frequency of the maximum amplitude $a_{\max}$ through all the sectors.

$$\mu_r = \frac{\sum_{n=1}^{N} |a_n - a_{\max}|/a_{\max}}{N}.100 \tag{15}$$

where a_n is the amplitude of the n^{th} sector and r is the rotational speed. This criterion, is calculated for all the Monte Carlo simulations and the average of all these values is calculated, serves to quantify the phenomenon of localisation as it measures the difference between the amplitude of each sector and the maximum sector amplitude. Therefore, an ACA close to 100 % means that only one sector vibrates with a large amplitude compared to the other sector, and an ACA close to 0 % means that all the sectors vibrate at the same amplitude, which is specific to travelling waves or nondegenerate modes. The third criterion is a discrete Fourier transform (DFT).

$$d_l = \frac{1}{N} \sum_{n=1}^{N} q_n e^{inl\theta} \tag{16}$$

where $\theta = 2\pi/N$, d_l is the coefficient of the l nodal diameter(s) component. An index l positive corresponds to a FW travelling wave, and a l negative corresponds to a BW travelling wave. q_n is the complex amplitude of the displacement of the n^{th} sector. In the presence of a perfect travelling wave response of l nodal diameters -which is the case of a tuned system with a rotating excitation with l EO- the coefficient d_l is equal to 1, and all the other coefficients different to l are equal to 0. When the response is strongly mistuned, there is the superposition of multiple travelling waves, and a few coefficients are different to 0. As for the second criterion, an average of all the Monte Carlo simulations is done to extract the average coefficients. These three criteria allow a quantification of the mistuning effect. The first gives information on the amplitude magnification (Eq. (14)), the second on the localisation (Eq. (15)) and the third on the presence or not of travelling waves (Eq. (16)).

4.4.1. Low modal density region

In the low modal density region with a 2EO-FW excitation, the amplitude magnification curve shapes change a lot between 0 rpm and 1,000 rpm. From 0 rpm to 100 rpm, the shape evolves from a curve with a peak at 1 % of mistuning level -green curve in Fig. 13- to a curve with a constant amplitude magnification increasing with the mistuning level -red curve in Fig. 13. From 100 rpm to 1,000 rpm the amplitude magnification values decrease significantly -blue curve in Fig. 13. After 1,000 rpm, these values remain almost constant (Fig. 14).

For the ACA criterion, the mistuning level (σ) has been fixed to 1 %, 5 %, and 10 %. The rotational speed range is zoomed between 0 rpm and 1,000 rpm as there is no significant change in behaviour after 1,000 rpm; the value at 10,000 rpm is considered as an asymptotic value. These values are indexed in Table 7. The ACA are maximal at 0 rpm for every mistuning level and decrease quickly with an increasing rotational speed until

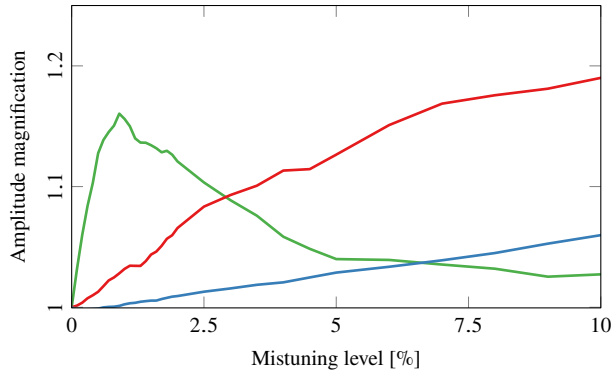

Figure 13: Variations in the amplitude magnification factor with mistuning in the low modal density region with a 2EO-FW excitation for different rotational speeds. For the green curve [—], the simulations have been carried-out at 0 rpm while for the red curve [—] and the blue curve [—] the simulations have been carried-out respectively at 100 rpm and 1,000 rpm.

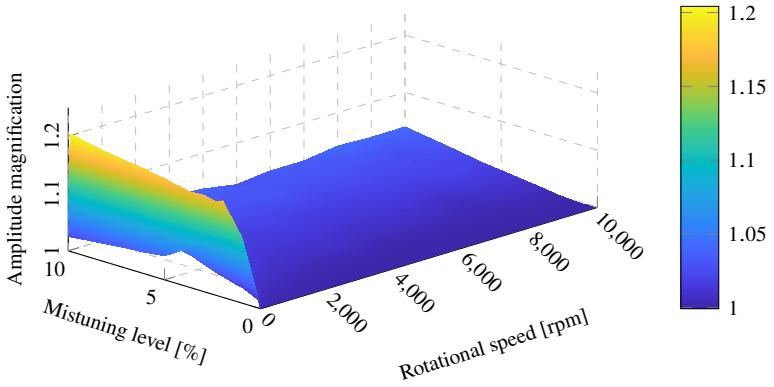

Figure 14: Variation in the amplitude magnification with the mistuning level and the rotational speed in the low modal density region with a 2EO-FW excitation.

1,000 rpm, then decrease slowly to reach a minimum value at 10,000 rpm, which shows that all the sectors vibrate with approximately the same amplitude at high speed, and that the minimum values reached depend on the mistuning level. The phenomenon of localisation is stronger with a high mistuning level and is more difficult to annihilate at high speed.

Table 7: Average change of amplitude at different rotational speeds in the low modal density region with a 2EO-FW excitation and different mistuning levels.

σ	μ_0	μ_{200}	μ_{400}	μ_{600}	μ_{800}	$\mu_{1,000}$	$\mu_{10,000}$
1 %	24.97	2.01	1.04	0.83	0.77	0.61	0.42
5 %	34.24	9.6	5.91	4.62	3.78	3.44	2.06
10 %	37.06	17.45	11.11	8.47	6.84	6.75	4.69

For the sake of clarity, the mistuning levels for the DFT criterion have been fixed to 1 % (Fig. 15a), 5 % (Fig. 15b), and 10 % (Fig. 15c). As for the ACA criterion, the rotational speed is zoomed between 0 rpm and 1,000 rpm. Only the 2ND-BW and 2ND-FW components can be observed in Fig. 15, as they are the only two significant components, all the other components being close to zero. At rest, the 2ND-BW and 2ND-FW components are close to each other, whereas when the speed increases, the 2ND-BW component decreases until it becomes negligible while the 2ND-FW component increases. Therefore, at speeds around 1,000 rpm and above, a full forward travelling wave of 2 nodal diameters is developed. As for the ACA criterion, the mistuning level does not change this behaviour. Although, it affects the values of the components. With

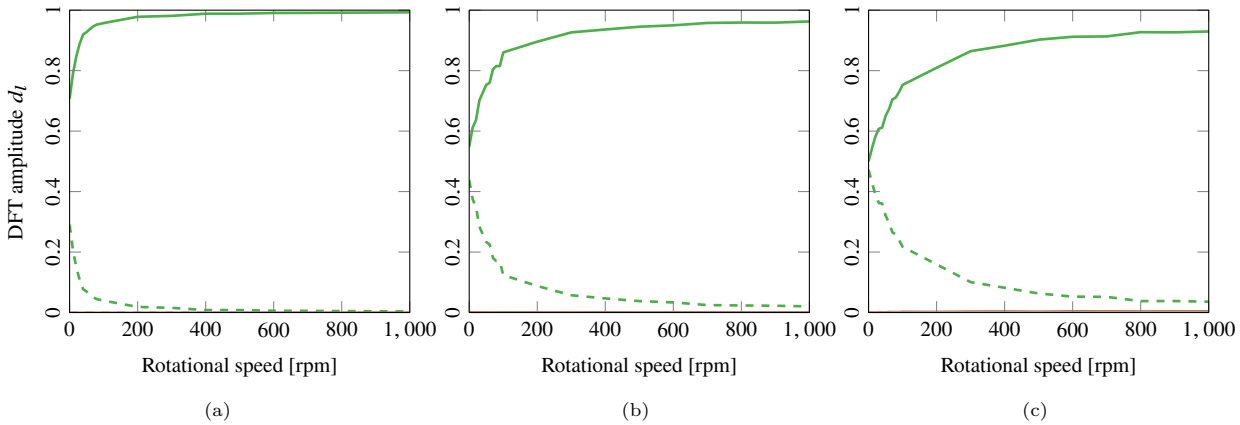

Figure 15: Evolution of the DFT components with speed in the low modal density region with a 2EO-FW excitation and different mistuning levels. (a) 1 % of mistuning level. (b) 5 % of mistuning level. (c) 10 % of mistuning level. The DFT components represent the participation of the different travelling waves on the dynamic response of the structure. In this case, only the components for the 2ND-BW [- -] and 2ND-FW [—] respond.

a higher mistuning level, the values of the 2ND-BW component decrease more slowly with an asymptotic value further away from zero, and the 2ND-FW increases more slowly with an asymptotic value less close to one. This means that the contribution of the 2ND-FW shape at high speed is less developed with a high mistuning level.

This behaviour, observed in a lumped model and analytically explained in [29], originates from the frequency isolation of modes due to the Coriolis effect. As there are no other nearby modes, the interaction of the tuned modes due to mistuning perturbation cannot develop, and therefore, the behaviour of the mistuned system is close to that of the tuned one.

4.4.2. High modal density region

For the high modal density region with a 6EO-FW excitation, the amplitude magnification is not perturbed by the rotational speed : the peak is always between 0.2 % and 0.3 % with maximum values between 1.3 and 1.35 (Fig. 16).

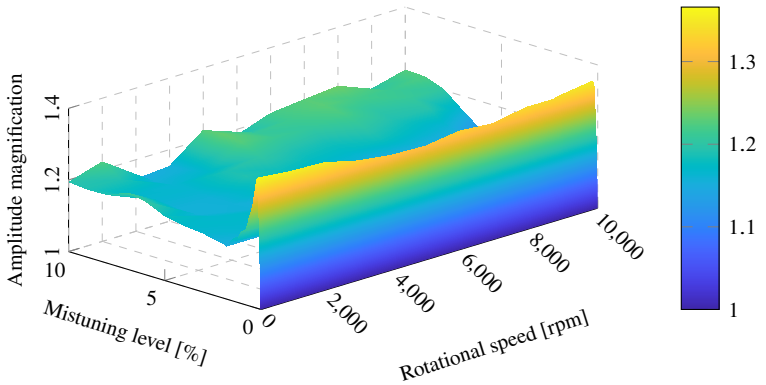

Figure 16: Variation in the amplitude magnification with the mistuning level and the rotational speed in the high modal density region with a 6EO-FW excitation.

The ACA criterion has been evaluated at the peak of the mistuning level, i.e., at 0.3 % and at 1 %, 5 %, 10 %. These values are indexed in Table 8 for different rotational speeds between 0 rpm and 10,000 rpm. As for the amplitude magnification, the ACA does not change significantly with the rotational speed. However, the localisation is not maximum at 0.3 % where the amplitude magnification is maximum. The localisation phenomenon is greater with a higher mistuning level.

Table 8: Average change of amplitude at different rotational speeds in the high modal density region with a 6EO-FW excitation and different mistuning levels.

σ	μ_0	$\mu_{2,000}$	$\mu_{4,000}$	$\mu_{6,000}$	$\mu_{8,000}$	$\mu_{10,000}$
0.3 %	52.54	52.82	51.87	52.1	50.4	50.11
1 %	66.11	68.31	67.44	66.23	66.16	66.96
5 %	81.83	79	80.99	82.16	79.39	79.35
10 %	86.02	83.24	83.21	84.45	84.26	83.88

In contrast to the DFT in the low modal density region, all the components have non-zero values in the high modal density region. Therefore, all the components are represented in Fig. 17 for 1 %, 5 %, and 10 % of the mistuning level. All the component values are below 0.1 except for the 6ND-FW component, which is slightly above. The participation of all the components in the forced response means that there is no specific travelling wave, which is compatible with the ACA criterion, which suggests a strong localisation of the response because of the mistuning perturbation. With a stronger mistuning level, all the DFT components converge to a restricted zone between 0.04 and 0.08, which reveals a stronger interaction of the modes due to the mistuning.

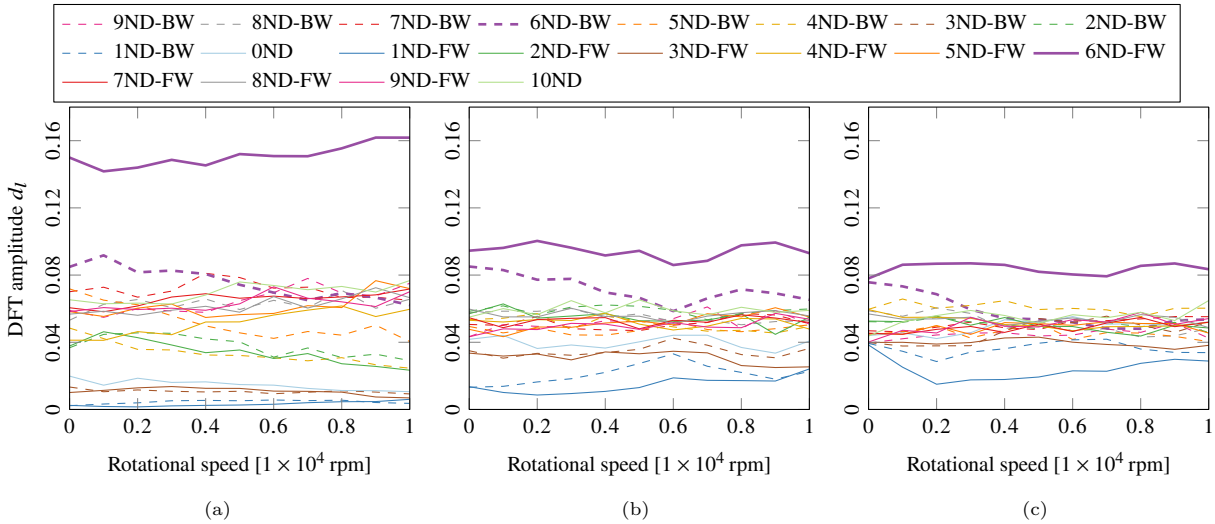

Figure 17: Evolution of the DFT components with speed in the high modal density region with a 6EO-FW excitation and different mistuning levels. (a) 1 % of mistuning level. (b) 5 % of mistuning level. (c) 10 % of mistuning level. The DFT components represent the participation of the different travelling waves on the dynamic response of the structure. The solid curves represent the forward wave [—] and the dashed curves represent the backward wave [- -].

These results show that the Coriolis effect has no impact on the forced response in a high modal density region. The localisation is stronger with a high mistuning level, even if the maximum amplitude magnification is at a low mistuning level.

4.4.3. Veering region

The amplitude magnification versus the mistuning level and rotational speed is plotted in Fig. 18 for the veering region with a 1EO-BW excitation. At 0 rpm, the maximum amplitude magnification is of 2.2 at 6 %. There are minor variations in the curve shapes between 0 rpm and 2,000 rpm, with a minimum amplitude magnification of 2 at 1,000 rpm and 4.5 % of the mistuning level. At 2000rpm and above, the curve shapes do not change, with a maximum amplitude magnification value between 2.1 and 2.3 for a mistuning level between 3 % and 3.5 %. It is interesting to mention that the growth due to the mistuning in the veering region in much slower than in the high modal density region (Fig. 17a). In the high modal density region, a small perturbation is sufficient to have a strong interaction between the modes as well as an amplitude magnification. In contrast, in the veering region, the modes are further apart from each other, so

there is a need for stronger mistuning to have an interaction between the modes and a significant amplitude magnification.

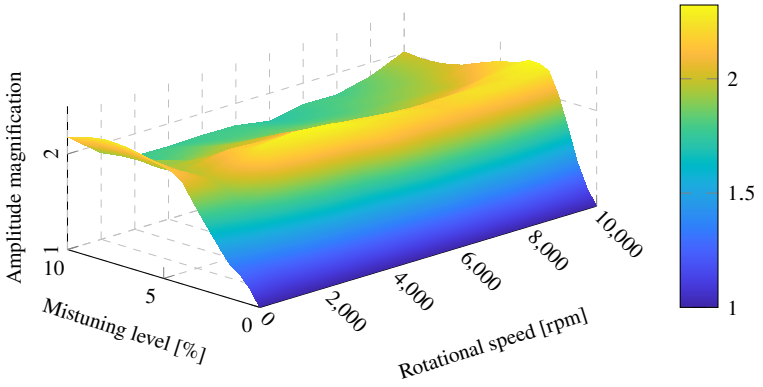

Figure 18: Variation in the amplitude magnification with the mistuning level and the rotational speed in the veering region with a 1EO-BW excitation.

The values of the ACA criterion are listed in Table 9 for 1 %, 3 %, 5 %, and 10 % of the mistuning level. The behaviour of this criterion is very similar to the high modal density region. These values do not change significantly with the rotational speed and increase with the mistuning level, although a decrease in the ACA at 2,000 rpm for 1 % of the mistuning level may be mentioned. This decrease is interpreted as a diminution of the mistuning localisation in this speed region with a low mistuning level.

Table 9: Average change of amplitude at different rotational speeds in the veering region with a 1EO-BW excitation and different mistuning levels.

	μ_0	$\mu_{2,000}$	$\mu_{4,000}$	$\mu_{6,000}$	$\mu_{8,000}$	$\mu_{10,000}$
1 %	42.12	26.96	34.19	38.81	39.88	31.45
3 %	65.43	65.51	74.01	74.38	76.67	72.97
5 %	78.65	77.34	82.89	82.4	83.75	81.91
10 %	87.76	82.72	84.34	86.54	86.54	86.98

As for the high modal density region, the DFT components in the veering region are non-zero values and are plotted in Fig. 19. At 0 rpm, the 1ND-FW and 1ND-BW components are equivalent and dominate compared to the other components, especially for a low mistuning level (Fig. 19a). At 2,000 rpm, only the 1ND-BW component is predominant, which means that there is a small diminution of the mistuning effect, in agreement with the ACA criterion. However, for higher mistuning levels (Fig. 19b and Fig. 19c), the 1ND-BW component values decrease and all the other components are present in the same range of values, between 0.02 and 0.08.

These results show that in the veering region with a 1EO-BW excitation, a full travelling wave cannot occur because of the mistuning and high modal density. It can be noted that at low speeds, the mistuning effects have a lower influence, with a major contribution by the 1ND-BW travelling wave Fig. 19a. There is a significant evolution of the dynamics with the rotational speed due to the proximity in frequency of the veering region with the high modal density region. Conversely, the 1ND-FW mode is present in the veering region at 0 rpm, but moves away with increasing rotational speed and becomes isolated in frequency.

The amplitude magnification versus the mistuning level and rotational speed is plotted in Fig. 20. Here, the mistuning level and the maximum amplitude magnification values are increasing with the rotational speed. At 0 rpm, the peak is at 6 % of the mistuning level for an amplitude magnification of 2.2 to reach 3.6 at 10 % and 4,000 rpm. Above this rotational speed, there is no peak below 10 % of the mistuning level and the amplitude magnification values decrease.

Here, the ACA criterion behaviour is like that of the low modal density region, with a decrease in the ACA values with the increasing rotational speed, and the values are higher with a higher mistuning level

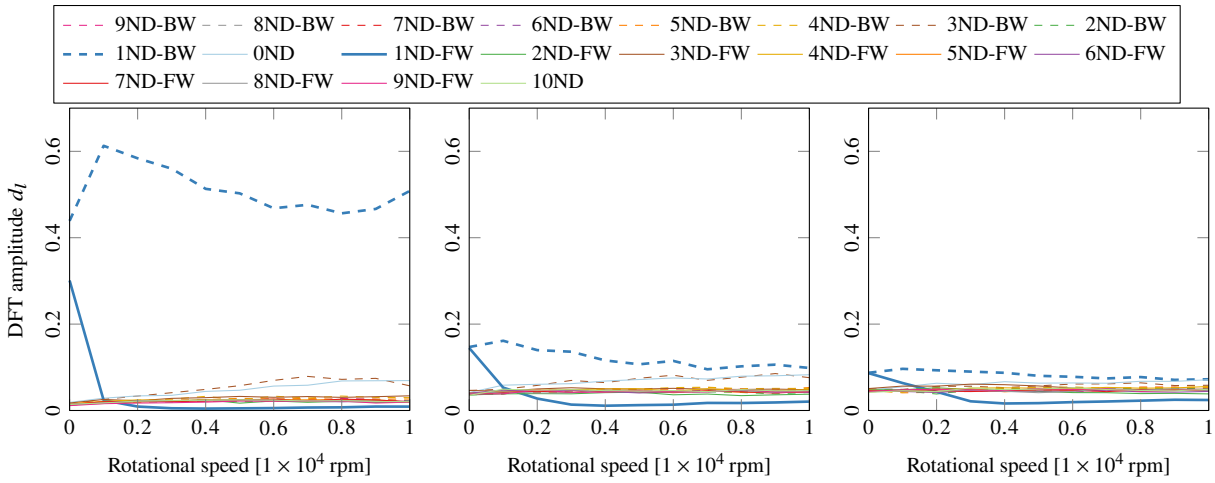

Figure 19: Evolution of the DFT components with speed in the veering region with a 1EO-BW excitation and different mistuning levels. (a) 1 % of mistuning level. (b) 5 % of mistuning level. (c) 10 % of mistuning level. The DFT components represent the participation of the different travelling waves on the dynamic response of the structure. The solid curves represent the forward wave [—] and the dashed curves represent the backward wave [- -].

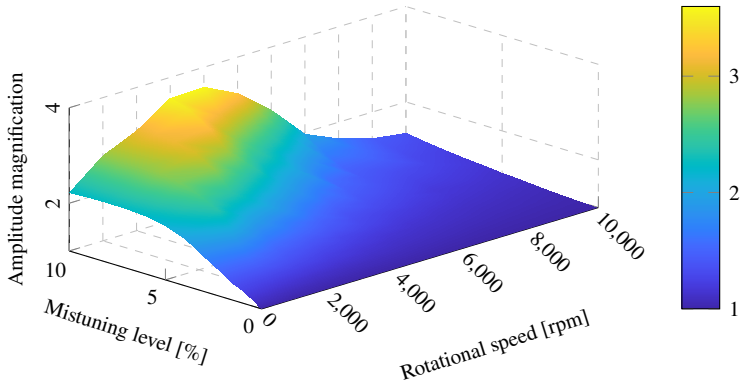

Figure 20: Variation in the amplitude magnification with the mistuning level and the rotational speed in the changing modal density region with a 1EO-FW excitation.

(Table 10). However, in this case, the decrease is not as fast as in the first case and the values for a high mistuning level are still high, so a strong localisation is still present.

Table 10: Average change of amplitude at different rotational speeds in the changing modal density region with a 1EO-FW excitation and different mistuning levels.

	μ_0	$\mu_{2,000}$	$\mu_{4,000}$	$\mu_{6,000}$	$\mu_{8,000}$	$\mu_{10,000}$
1 %	42.3	13.42	8.19	5.23	3.3	2.33
5 %	78.42	59.29	41.18	26.61	16.17	11.8
10 %	87.76	83.57	73.3	54.62	34.74	24.24

The DFT at 1 %, 5 % and 10 % of the mistuning level plotted in Fig. 21 confirms the behaviour of the ACA criterion. At 0 rpm, all the components are non-negligible and the 1ND-BW and 1ND-FW components are predominant. Then the 1ND-FW component increases with the increasing rotational speed while the other components become almost negligible, which reveals the appearance of a distinct 1ND-FW shape response. With the mistuning level higher, the phenomenon becomes less pronounced.

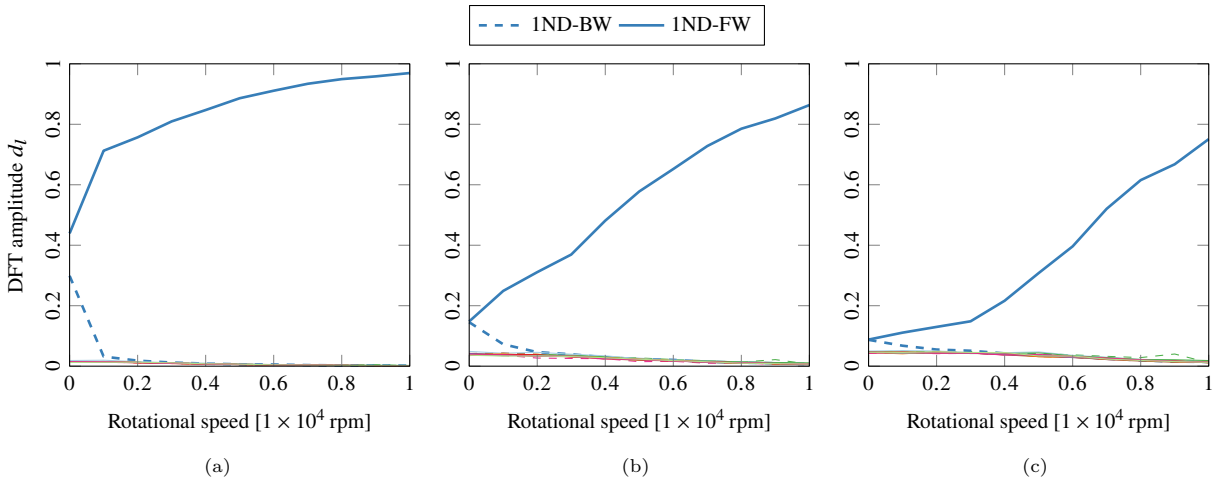

Figure 21: Evolution of the DFT components with speed in the changing modal density region with a 1EO-FW excitation and different mistuning levels. (a) 1 % of mistuning level. (b) 5 % of mistuning level. (c) 10 % of mistuning level. The DFT components represent the participation of the different travelling waves on the dynamic response of the structure. In this case, the components for the 1ND-BW [- -] and 1ND-FW [—] mostly respond. All the other components respond at the same low level.

From these results, it can be concluded that the large mistuning effects present in the veering region at rest can be reduced if the natural frequency moves away from the veering region with increased rotational speeds, due to the Coriolis effect. In this mistuning case, a travelling wave response with a behaviour close to the tuned case can be observed, but the 1ND-FW pureness response depends on the mistuning level. When the natural frequency stays close to the veering region, there are no particular changes in the behaviour: the mistuning effect remains predominant.

5. Conclusions

The main objective of this paper was to investigate the interactions between the Coriolis and mistuning effects on bladed drums and the predominance of one effect over the other. A FEM of a simplified industrial bladed drum was used to carry out a forced response statistic analysis using Monte Carlo simulations at different mistuning levels and rotational speeds. To that end, an overview of the SNM, CMM and IMM methods was given since these methods were selected to construct the different ROMs of the mistuned bladed drum accounting for the Coriolis effect.

The blade mistuning is the main driver of the response behaviour, especially for blade-dominated modes but also for blade-disc modes in veering regions. The only exception is for disc-dominated modes for which the disc mistuning governs the response behaviour. In all cases, the sector mistuning always follows the dominant behaviour and therefore the IMM method is the most convenient for models with high disc participation.

The present work clearly shows that it is important to take the Coriolis effect into account when studying the disc modes or the veering regions since their behaviour is completely different when the Coriolis effect is not taken into account. The only case where it is possible to neglect the Coriolis matrix is with the blade-dominated modes for which the disc dynamics has a small impact on the global response.

The interaction between Coriolis and mistuning was investigated with the evolution of the rotational speed in three different regions. In the low modal density region, the mode quickly becomes isolated in frequency from the other modes because of the Coriolis effect, which results in a travelling wave and a behaviour similar to that of the tuned case. In the high modal density region, the localisation and amplitude magnification are strong and do not change significantly with the rotational speed due to the lack of influence of the Coriolis effect. When the mode stays close to the veering region, the mistuning remains unaffected by the rotational speed, but when it moves away from the veering region, a travelling wave similar to that observed in the tuned behaviour appears.

The validation of ROMs with the Coriolis effect has been done for only three different methods, the SNM, CMM and IMM. It would be interesting to adapt and validate other methods including the Coriolis effect

[35, 37, 39, 40]. It may be especially useful to investigate the NEWT [41] method, as it is one of the most recent methods for the reduction of mistuned bladed discs and can be used to increase accuracy compared to the CMM and IMM thanks to the use of sector-level modes for the mistuning projection.

Investigations of the Coriolis effect and mistuning interactions have been focused on small mistuning methods only. It would be efficient to extend these investigations to large mistuning, detuning or geometric mistuning and the use of reduction methods like the MMDA [55], Mbaye's method [56], PRIME [57], N-PRIME [58], PRISM [59], as well as for nonlinear methods with the CNCMS [60] and SNCR [61].

The development of the IMM method in a state-space representation to take the Coriolis effect directly into account in the reduction basis will be the subject of future work. The calculation time for the reduction basis may be much larger, as has already been shown in this article, but taking the Coriolis effect into account in the calculation of the tuned modes and free-interface sector modes may also potentially increase the accuracy of the forced response and allow one to decrease the size of the ROM. The time lost during the computation of the ROM can be made up for with the Monte Carlo simulation.

CRediT authorship contribution statement

Anthony Tacher: Methodology, Software, Formal analysis, Writing - Original Draft, Writing - Review & Editing **Fabrice Thouverez:** Conceptualisation, Resources, Writing - Review & Editing, Supervision, Funding acquisition **Jason Armand:** Validation, Resources, Writing - Review & Editing, Supervision, Funding acquisition

Declaration of Competing Interest

The authors declare that they have no known competing financial interests or personal relationships that could have appeared to influence the work reported in this paper.

Acknowledgements

The authors are thankful to Safran Tech for providing the financial support for this project, and for giving permission to publish this work.

Appendix A. Matrix expressions

$$\mathbf{M} = \int_{\mathcal{V}} \rho \mathbf{H}^\intercal \mathbf{H} V \tag{A.1}$$

$$\mathbf{C} = \alpha \int_{\mathcal{V}} \rho \mathbf{H}^\intercal \mathbf{H} V + \beta \int_{\mathcal{V}} (\nabla \mathbf{H})^\intercal \mathbf{D} (\nabla \mathbf{H}) V \tag{A.2}$$

$$\mathbf{G} = 2 \int_{\mathcal{V}} \rho \mathbf{H}^\intercal \mathbf{\Omega} \mathbf{H} V \tag{A.3}$$

$$\mathbf{K}_{\mathrm{l}} = \int_{\mathcal{V}} (\nabla \mathbf{H})^\intercal \mathbf{D} (\nabla \mathbf{H}) V \tag{A.4}$$

$$\mathbf{K}_{\mathrm{s}} = \int_{\mathcal{V}} \rho \mathbf{H}^\intercal \mathbf{\Omega}^2 \mathbf{H} V \tag{A.5}$$

$$\mathbf{K}_{\mathrm{g}}(\mathbf{q}_{\mathrm{st}}) = \frac{\partial \mathbf{f}^{\mathrm{q}}}{\partial \mathbf{q}}(\mathbf{q}_{\mathrm{st}}) + \frac{\partial \mathbf{f}^{\mathrm{c}}}{\partial \mathbf{q}}(\mathbf{q}_{\mathrm{st}}) \tag{A.6}$$

$$\mathbf{f}^{\mathrm{q}}(\mathbf{q}) = \int_{\mathcal{V}} (\nabla_{\mathbf{q}} \mathbf{H}\mathbf{q})^\intercal \mathbf{C} (\nabla \mathbf{H}) \mathbf{q} V + \frac{1}{2} \int_{\mathcal{V}} (\nabla \mathbf{H})^\intercal \mathbf{C} (\nabla_{\mathbf{q}} \mathbf{H}\mathbf{q}) \mathbf{q} V \tag{A.7}$$

$$\mathbf{f}^{\mathrm{c}}(\mathbf{q}) = \frac{1}{2} \int_{\mathcal{V}} (\nabla_{\mathbf{q}} \mathbf{H}\mathbf{q})^\intercal \mathbf{C} (\nabla_{\mathbf{q}} \mathbf{H}\mathbf{q}) \mathbf{q} V \tag{A.8}$$

where $\mathbf{H}$ is the matrix of shape functions (the expressions of the shape functions for a 20-nodes element can be found in [62]), $\mathbf{D}$ the matrix of elasticity, $\mathbf{\Omega}$ the rotational matrix, ∇ the linear differential operator and $\nabla_{\mathbf{q}}$ the nonlinear differential operator. The developments and expressions of these matrices and operators can be found in [45].

Appendix B. Developpement of the reduction techniques for the Coriolis and mistuning effects

Appendix B.1. Subset of Nominal system Modes (SNM)

Consider the classical equation of motion of a bladed disc mistuned system :

$$\mathbf{M}\ddot{\mathbf{q}} + (\mathbf{C} + \mathbf{G})\dot{\mathbf{q}} + \mathbf{K}\mathbf{q} = \mathbf{f}_{\text{ext}} \tag{B.1}$$

In the case of stiffness mistuning only, there are:

$$\mathbf{K} = \mathbf{K}^0 + \Delta\mathbf{K} \tag{B.2}$$

$\mathbf{K}^0$ is the stiffness matrix of the tuned model and $\Delta\mathbf{K}$ is the stiffness perturbation.

The SNM method is based on the assumption that the unknown displacement vector for a small mistuned model can be approximated as a subset of the tuned modes.

$$\mathbf{q} \approx \Phi^0\mathbf{p} \tag{B.3}$$

where $\mathbf{p}$ is the new reduced unknown vector and in which each term determines the contribution of each tuned mode in the response. Φ^0 and Λ^0 are the chosen eigenvectors and eigenvalues used for the subset of nominal modes and which satisfy the system

$$\mathbf{K}^0\Phi^0 = \mathbf{M}\Phi^0\Lambda^0 \tag{B.4}$$

Therefore, the equation of motion of the mistuned system Eq. (B.1) can be reduced on a subset of nominal modes composed of the tuned modes located in a frequency range of interest and by premultiplying Eq. (B.1) by ${\Phi^0}^{\mathsf{H}}$ the Hermitian of Φ^0

$$\ddot{\mathbf{p}} + (\hat{\mathbf{C}} + \hat{\mathbf{G}})\dot{\mathbf{p}} + (\Lambda^0 + {\Phi^0}^{\mathsf{H}}\Delta\mathbf{K}\Phi^0)\mathbf{p} = \hat{\mathbf{f}}_{\text{ext}} \tag{B.5}$$

where

$${\Phi^0}^{\mathsf{H}}\mathbf{M}\Phi^0 = \mathbf{I} \tag{B.6}$$

$${\Phi^0}^{\mathsf{H}}\mathbf{C}\Phi^0 = \hat{\mathbf{C}} \tag{B.7}$$

$${\Phi^0}^{\mathsf{H}}\mathbf{G}\Phi^0 = \hat{\mathbf{G}} \tag{B.8}$$

$${\Phi^0}^{\mathsf{H}}\mathbf{K}^0\Phi^0 = \Lambda^0 \tag{B.9}$$

$${\Phi^0}^{\mathsf{H}}\mathbf{f}_{\text{ext}} = \hat{\mathbf{f}}_{\text{ext}} \tag{B.10}$$

Appendix B.2. Component Mode Mistuning (CMM)

The constraint modes Ψ_{CB} used in the CMM are obtained by applying a unit displacement to each dof of the blade-disc interface while keeping the other dofs fixed. It follows that they can be determined using the following equation:

$$\Psi_{\text{CB}} = -{\mathbf{K}_{\text{ii}}^{\text{b}}}^{-1}\mathbf{K}_{\text{ic}}^{\text{b}} \tag{B.11}$$

where superscript b illustrates the tuned blade and subscripts i and c indicate the internal blade dofs and the boundary blade dofs.

The projection of the mistuned matrix onto the chosen eigenvectors Φ_{CB} and constraint modes Ψ_{CB} is very similar to the Craig-Bampton transformation [12].

$$\Phi_n^{\text{b}} = \begin{bmatrix}\Phi_{n,\text{i}}^{\text{b}} \\ \Phi_{n,\text{c}}^{\text{b}}\end{bmatrix} \approx \begin{bmatrix}\Phi_{\text{CB}} & \Psi_{\text{CB}} \\ \mathbf{0} & \mathbf{I}\end{bmatrix}\begin{bmatrix}\mathbf{Q}_n^{\Phi_{\text{CB}}} \\ \mathbf{Q}_n^{\Psi_{\text{CB}}}\end{bmatrix} = \mathbf{T}_{\text{CB}}\mathbf{Q}_n \tag{B.12}$$

where Φ_n^{b} is the matrix of the tuned modes limited to the blade dofs of the n^{th} sector. $\mathbf{Q}_n^{\Phi_{\mathrm{CB}}}$ and $\mathbf{Q}_n^{\Psi_{\mathrm{CB}}}$ are respectively the modal participation factors of the cantilevered tuned blade modes and constraint modes for the blade of the n^{th} sector. The participation factors matrix can be found directly with Eq. (B.12)

$$\mathbf{Q}_n^{\Psi_{\mathrm{CB}}} = \Phi_{n,\mathrm{c}}^{\mathrm{b}} \tag{B.13}$$

Premultiplying Eq. (B.12) by $\left(\begin{bmatrix}\Phi_{\mathrm{CB}}\\ \mathbf{0}\end{bmatrix}^{\mathsf{H}} \mathbf{K}^{\mathrm{b}}\right)$ and using the orthogonality of the modes serves to determine the expression of $\mathbf{Q}_n^{\Phi_{\mathrm{CB}}}$

$$\mathbf{Q}_n^{\Phi_{\mathrm{CB}}} = \Lambda_{\mathrm{CB}}^{-1} \begin{bmatrix}\Phi_{\mathrm{CB}}\\ \mathbf{0}\end{bmatrix}^{\mathsf{H}} \mathbf{K}^{\mathrm{b}} \Phi_n^{\mathrm{b}} \tag{B.14}$$

where Λ_{CB} is the diagonal matrix of the cantilevered tuned blade eigenvalues. As the mistuning is only considered for the blade stiffening perturbation, the matrix $\mathbf{\Delta K}$ is block diagonal and its reduction can be expressed as the following sum:

$$\Phi^{0\mathsf{H}} \mathbf{\Delta K} \Phi^0 = \sum_{n=1}^{N} \Phi_n^{\mathrm{b}\,\mathsf{H}} \mathbf{\Delta K}_n^{\mathrm{b}} \Phi_n^{\mathrm{b}} \tag{B.15}$$

where $\mathbf{\Delta K}_n^{\mathrm{b}}$ is the stiffness mistuning perturbation of the n^{th} blade. Substituting Eq. (B.12) in Eq. (B.15) gives

$$\Phi^{0\mathsf{H}} \mathbf{\Delta K} \Phi^0 \approx \sum_{n=1}^{N} \mathbf{Q}_n{}^{\mathsf{H}} \mathbf{T}_{\mathrm{CB}}{}^{\mathsf{H}} \mathbf{\Delta K}_n^{\mathrm{b}} \mathbf{T}_{\mathrm{CB}} \mathbf{Q}_n \tag{B.16}$$

The mistuning is considered proportional, as follows:

$$\mathbf{\Delta K}_n^{\mathrm{b}} = \delta_n \mathbf{K}^{\mathrm{b}} \tag{B.17}$$

At rest, this definition of proportional mistuning may be due to a variation of Young's modulus [35]. It is now possible to simplify Eq. (B.16)

$$\Phi^{0\mathsf{H}} \mathbf{\Delta K} \Phi^0 \approx \sum_{n=1}^{N} \delta_n \mathbf{Q}_n{}^{\mathsf{H}} \mathbf{T}_{\mathrm{CB}}{}^{\mathsf{H}} \mathbf{K}^{\mathrm{b}} \mathbf{T}_{\mathrm{CB}} \mathbf{Q}_n \tag{B.18}$$

Appendix B.3. Integral Mode Mistuning (IMM)

With a sector mistuning, the mistuning stiffness matrix $\mathbf{\Delta K}$ is no longer block diagonal, but it is still possible to express its reduction as a sum:

$$\Phi^{0\mathsf{H}} \mathbf{\Delta K} \Phi^0 = \sum_{n=1}^{N} \Phi_n^{\mathrm{s}\,\mathsf{H}} \mathbf{\Delta K}_n^{\mathrm{s}} \Phi_n^{\mathrm{s}} \tag{B.19}$$

where $\mathbf{\Delta K}_n^{\mathrm{s}}$ is the stiffness perturbation matrix, and Φ_n^{s} the subset of tuned modes matrix restrained to the n^{th} sector, including the left (l) and right (r) interfaces dofs.

$$\Phi_n^{\mathrm{s}\,\mathsf{H}} \mathbf{\Delta K}_n^{\mathrm{s}} \Phi_n^{\mathrm{s}} = \begin{bmatrix}\Phi_{n,\mathrm{r}}^{\mathrm{s}}\\ \Phi_{n,\mathrm{i}}^{\mathrm{s}}\\ \Phi_{n,\mathrm{l}}^{\mathrm{s}}\end{bmatrix}^{\mathsf{H}} \begin{bmatrix}\mathbf{\Delta K}_{n,\mathrm{rr}}^{\mathrm{s}} & \mathbf{\Delta K}_{n,\mathrm{ri}}^{\mathrm{s}} & \mathbf{0}\\ \mathbf{\Delta K}_{n,\mathrm{ir}}^{\mathrm{s}} & \mathbf{\Delta K}_{n,\mathrm{ii}}^{\mathrm{s}} & \mathbf{\Delta K}_{n,\mathrm{il}}^{\mathrm{s}}\\ \mathbf{0} & \mathbf{\Delta K}_{n,\mathrm{li}}^{\mathrm{s}} & \mathbf{\Delta K}_{n,\mathrm{ll}}^{\mathrm{s}}\end{bmatrix} \begin{bmatrix}\Phi_{n,\mathrm{r}}^{\mathrm{s}}\\ \Phi_{n,\mathrm{i}}^{\mathrm{s}}\\ \Phi_{n,\mathrm{l}}^{\mathrm{s}}\end{bmatrix} \tag{B.20}$$

The tuned modes Φ_n^{s} are express as a linear combination of the free-interface sector modes Φ^{FS} using participation factors $\mathbf{Q}_n$

$$\Phi_n^{\mathrm{s}} \approx \Phi^{\mathrm{FS}} \mathbf{Q}_n \tag{B.21}$$

Premultiplying Eq. (B.21) with $\left(\Phi^{\mathrm{FS}\mathsf{H}} \mathbf{K}^{\mathrm{FS}}\right)$ where $\mathbf{K}^{\mathrm{FS}}$ is the stiffness matrix of the tune free-interface sector, and using the orthogonality of the modes serves to determine the expression of $\mathbf{Q}_n$

$$\mathbf{Q}_n = \Lambda^{\mathrm{FS}\,-1} \Phi^{\mathrm{FS}\mathsf{H}} \mathbf{K}^{\mathrm{FS}} \Phi_n^{\mathrm{s}} \tag{B.22}$$

where Λ^{FS} is the diagonal matrix of the free-interface sector eigenvalues. Replacing Eq. (B.21) in Eq. (B.19), and using proportional mistuning gives

$$\Phi^{0\mathsf{H}}\Delta\mathbf{K}\Phi^{0} \approx \sum_{n=1}^{N} \delta_n \mathbf{Q}_n{}^{\mathsf{H}} \Lambda^{FS} \mathbf{Q}_n \tag{B.23}$$

Appendix C. Excitation force and damping matrix for the forced response simulations

First, the excitation introduced in the simulations will always be a rotating force excitation. This excitation has the same amplitude $\mathbf{f}_{\mathrm{A}}$ for the same dof of each sector with a phase which depends on EO k, sector number n, and excitation frequency ω.

$$\mathbf{f}_{\mathrm{ext}}^{n} = \mathbf{f}_{\mathrm{A}} e^{i(\omega t-(n-1)\theta k)} \tag{C.1}$$

Where $\theta = 2\pi/N$ and, as for the nodal diameters, a k positive corresponds to a forward travelling wave excitation and a k negative to a backward travelling wave excitation. The excited dof and the excitation vector $\mathbf{f}_{\mathrm{A}}$ are represented in Fig. 2b.

For the forced response, a damping matrix $\mathbf{C}$ is introduced in the equation of motion, which is defined as follows:

$$\mathbf{C} = \alpha\mathbf{M} + \beta\mathbf{K} \tag{C.2}$$

Where coefficients α and β are calculated using a damping ratio $\xi = 5e^{-4}$ and the first natural frequency of the tune model $\omega_0 = 319.62$ Hz.

$$\alpha = 2\pi\xi\omega_0 \tag{C.3}$$

$$\beta = \frac{\xi}{2\pi\omega_0} \tag{C.4}$$

References

[1] D. L. Thomas, Dynamics of rotationally periodic structures, International Journal for Numerical Methods in Engineering 14 (1) (1979) 81–102. doi:10.1002/nme.1620140107.

[2] L. E. El-Bayoumy, A. V. Srinivasan, Influence of mistuning on rotor-blade vibrations, AIAA Journal 13 (4) (1975) 460–464. doi:10.2514/3.49731.

[3] S.-T. Wei, C. Pierre, Localization phenomena in mistuned assemblies with cyclic symmetry part I: free vibrations, Journal of Vibration, Acoustics, Stress, and Reliability in Design 110 (4) (1988) 429–438. doi:10.1115/1.3269547.

[4] S.-T. Wei, C. Pierre, Localization phenomena in mistuned assemblies with cyclic symmetry part ii: Forced vibrations, Journal of Vibration, Acoustics, Stress, and Reliability in Design 110 (4) (1988) 439–449. doi:10.1115/1.3269548.

[5] K. B. Subrahmanyam, K. R. V. Kaza, Non-linear flap-lag-extensional vibrations of rotating, pretwisted, preconed beams including Coriolis effects, International journal of mechanical sciences 29 (1) (1987) 29–43. doi:10.1016/0020-7403(87)90072-5.

[6] M. Nikolic, E. P. Petrov, D. J. Ewins, Coriolis forces in forced response analysis of mistuned bladed disks, Journal of turbomachinery 129 (4) (2007) 730–739. doi:10.1115/1.2720866.

[7] C. Gibert, V. Kharyton, F. Thouverez, P. Jean, On forced response of a rotating integrally bladed disk: Predictions and experiments, in: ASME turbo expo 2010: Power for land, sea, and air, ASME, 2010. doi:10.1115/GT2010-23610.

[8] Z. Qin, Z. Yang, J. Zu, F. Chu, Free vibration analysis of rotating cylindrical shells coupled with moderately thick annular plates, International Journal of Mechanical Sciences 142 (2018) 127–139. doi:10.1016/j.ijmecsci.2018.04.044.

[9] C. Li, Q. Tang, C. Xi, B. Zhong, B. Wen, Coupling vibration behaviors of drum-disk-shaft structures with elastic connection, International Journal of Mechanical Sciences 155 (2019) 392–404. doi:10.1016/j.ijmecsci.2019.03.014.

[10] Q. Tang, C. Li, H. She, B. Wen, Analysis of frequency and mode shape of rotating-flexible disk-drum coupled structure with non-continuous connections, International Journal of Mechanical Sciences 190 (2021) 106004. doi:10.1016/j.ijmecsci.2020.106004.

[11] J. Wildheim, Excitation of rotating circumferentially periodic structures, Journal of Sound and Vibration 75 (3) (1981) 397–416. doi:10.1016/0022-460x(81)90386-2.

[12] R. R. Craig Jr., M. C. C. Bampton, Coupling of substructures for dynamic analyses., AIAA journal 6 (7) (1968) 1313–1319. doi:10.2514/3.4741.

[13] J. Yuan, F. Scarpa, G. Allegri, B. Titurus, S. Patsias, R. Rajasekaran, Efficient computational techniques for mistuning analysis of bladed discs: A review, Mechanical Systems and Signal Processing 87 (2017) 71–90. doi:10.1016/j.ymssp.2016.09.041.

[14] C. U. Waldherr, D. M. Vogt, An Extension of the Classical Subset of Nominal Modes Method for the Model Order Reduction of Gyroscopic Systems, Journal of Engineering for Gas Turbines and Power 141 (5), 052501 (12 2018). doi:10.1115/1.4041117.

[15] S. Wang, C. Bi, B. Zi, C. Zheng, Vibration characteristics of rotating mistuned bladed disks considering the coriolis force, spin softening, and stress stiffening effects, Shock and Vibration 2019 (2019). doi:10.1155/2019/9714529.

[16] X. Yan, W. Sun, D. Du, K. Xu, Effects of nonlinear coatings on vibration characteristics of rotating blisks with mistuning features, Engineering Failure Analysis 128 (2021) 105632. doi:10.1016/j.engfailanal.2021.105632.

[17] H. Zhang, H. Yuan, H. Sun, Effect of Coriolis force on vibration localization characteristics of mistuned bladed disk, Journal of Vibroengineering 22 (5) (2020) 1069–1083. doi:10.21595/jve.2020.21237.

[18] H. Zhang, H. Yuan, H. Sun, Vibration reduction optimization for mistuned bladed disk based on reduced order modeling technique, Journal of Vibroengineering 23 (2) (2021) 385–399. doi:10.21595/jve.2020.21381.

[19] M.-T. Yang, J. H. Griffin, A reduced-order model of mistuning using a subset of nominal system modes, J. Eng. Gas Turbines Power 123 (4) (2001) 893–900. doi:10.1115/1.1385197.

[20] S.-H. Lim, R. Bladh, M. P. Castanier, C. Pierre, Compact, generalized component mode mistuning representation for modeling bladed disk vibration, AIAA journal 45 (9) (2007) 2285–2298. doi:10.2514/1.13172.

[21] P. Vargiu, C. M. Firrone, S. Zucca, M. M. Gola, A reduced order model based on sector mistuning for the dynamic analysis of mistuned bladed disks, International Journal of Mechanical Sciences 53 (8) (2011) 639–646. doi:10.1016/j.ijmecsci.2011.05.010.

[22] B. W. Huang, J. H. Kuang, Mode localization in a rotating mistuned turbo disk with Coriolis effect, International journal of mechanical sciences 43 (7) (2001) 1643–1660. doi:10.1016/S0020-7403(00)00096-5.

[23] P. Almeida, C. Gibert, X. Leblanc, J.-P. Ousty, F. Thouverez, Experimental and numerical investigations on a rotating centrifugal compressor, in: ASME Turbo Expo 2012: Turbine Technical Conference and Exposition, American Society of Mechanical Engineers, 2012, pp. 1133–1142. doi:10.1115/GT2012-69760.

[24] V. Ruffini, J. S. Green, C. W. Schwingshackl, The Influence of Mistuning and Coriolis Effects on the Modal Parameters of Bladed Discs: An Experimental Study, in: ASME Turbo Expo 2017: Turbomachinery Technical Conference and Exposition, American Society of Mechanical Engineers, 2017. doi:10.1115/GT2017-63437.

[25] J. Xin, J. Wang, Investigation of coriolis effect on vibration characteristics of a realistic mistuned bladed disk, in: ASME 2011 turbo expo: Turbine technical conference and exposition, American Society of Mechanical Engineers, 2011, pp. 993–1005. doi:10.1115/1.2720866.

[26] X. Kan, Z. Xu, Vibration localization for a rotating mistuning bladed disk with the Coriolis effect by a state-space decoupling method, Proceedings of the Institution of Mechanical Engineers, Part G: Journal of Aerospace Engineering 233 (3) (2017) 1011–1020. doi:10.1177/0954410017744238.

[27] X. Kan, B. Zhao, Vibration characteristics of a mistuned bladed disk considering the effect of Coriolis forces, Shock and Vibration 2016 (2016). doi:10.1155/2016/4656032.

[28] X. Kan, Z. Xu, B. Zhao, J. Zhong, Effect of Coriolis force on forced response magnification of intentionally mistuned bladed disk, Journal of Sound and Vibration 399 (2017) 124–136. doi:10.1016/j.jsv.2017.03.002.

[29] A. Tacher, F. Thouverez, J. Armand, Interaction Between Coriolis Forces and Mistuning on a Cyclic Symmetric Structure With Geometrical Nonlinearity, Journal of Engineering for Gas Turbines and Power 143 (5), 051006 (03 2021). doi:10.1115/1.4048844.

[30] M. Castanier, C. Pierre, Investigation of the combined effects of intentional and random mistuning on the forced response of bladed disks, in: 34th AIAA/ASME/SAE/ASEE Joint Propulsion Conference and Exhibit, 1998, p. 3720. doi:10.2514/6.1998-3720.

[31] M. P. Mignolet, W. Hu, I. Jadic, On the forced response of harmonically and partially mistuned bladed disks. Part II: partial mistuning and applications, International Journal of Rotating Machinery 6 (1) (2000) 43–56. doi:10.1155/s1023621x00000051.

[32] M. P. Castanier, C. Pierre, Using intentional mistuning in the design of turbomachinery rotors, AIAA journal 40 (10) (2002) 2077–2086. doi:10.2514/2.1542.

[33] M. I. Hussein, M. P. Castanier, C. Pierre, Examination of the relationship between tuned free vibration characteristics and mistuning sensitivity for an industrial turbomachinery rotor, Tech. rep., The University of Michigan (2001).

[34] R. Bladh, C. Pierre, M. P. Castanier, M. J. Kruse, Dynamic response predictions for a mistuned industrial turbomachinery rotor using reduced-order modeling, J. Eng. Gas Turbines Power 124 (2) (2002) 311–324. doi:10.1115/1.1447236.

[35] R. Bladh, M. P. Castanier, C. Pierre, Component-Mode-Based Reduced Order Modeling Techniques for Mistuned Bladed Disks—Part I: Theoretical models, Journal of Engineering for Gas Turbines and Power 123 (1) (2001) 89–99. doi:10.1115/1.1338947.

[36] R. Bladh, M. P. Castanier, C. Pierre, Component-Mode-Based Reduced Order Modeling Techniques for Mistuned Bladed Disks—Part II: Application , Journal of Engineering for Gas Turbines and Power 123 (1) (2001) 100–108. doi:10.1115/1.1338948.

[37] E. P. Petrov, K. Y. Sanliturk, D. J. Ewins, A new method for dynamic analysis of mistuned bladed disks based on the exact relationship between tuned and mistuned systems, J. Eng. Gas Turbines Power 124 (3) (2002) 586–597. doi:10.1115/1.1451753.

[38] M.-T. Yang, J. H. Griffin, A Reduced Order Approach for the Vibration of Mistuned Bladed Disk Assemblies, Journal of Engineering for Gas Turbines and Power 119 (1) (1997) 161–167. doi:10.1115/1.2815542.

[39] D. M. Feiner, J. H. Griffin, A fundamental model of mistuning for a single family of modes, J. Turbomach. 124 (4) (2002) 597–605. doi:10.1115/1.1508384.

[40] C. Martel, R. Corral, J. M. Llorens, Stability increase of aerodynamically unstable rotors using intentional mistuning, Journal of Turbomachinery 130 (1) (2008). doi:10.1115/1.2720503.

[41] C. Fitzner, B. I. Epureanu, S. Filippi, Nodal energy weighted transformation: A mistuning projection and its application to FLADE™ turbines, Mechanical Systems and Signal Processing 42 (1-2) (2014) 167–180. doi:10.1016/j.ymssp.2013.08.027.

[42] A. Sternchüss, Multi-level parametric reduced models of rotating bladed disk assemblies, Ph.D. thesis, Châtenay-Malabry, Ecole centrale de Paris (2009).

[43] T. J. Ypma, Historical Development of the Newton–Raphson Method, SIAM Review 37 (4) (1995) 531–551. doi:10.1137/1037125.

[44] R. Bladh, M. P. Castanier, C. Pierre, Reduced Order Modeling and Vibration Analysis of Mistuned Bladed Disk Assemblies With Shrouds, Journal of Engineering for Gas Turbines and Power 121 (3) (1999) 515–522. doi:10.1115/1.2818503.

[45] V. Ruffini, Coriolis effects in bladed discs, Ph.D. thesis, Imperial College London (2016). doi:10.25560/61825.

[46] C. Pierre, Mode localization and eigenvalue loci veering phenomena in disordered structures, Journal of Sound and Vibration 126 (3) (1988) 485–502. doi:10.1016/0022-460x(88)90226-x.

[47] C. Lein, M. Beitelschmidt, Comparative study of model correlation methods with application to model order reduction, in: Proceedings 26th ISMA (International Conference on Noise and Vibration Engineering), 2014, pp. 2683–2700.

[48] I. Bucher, D. J. Ewins, Modal analysis and testing of rotating structures, Philosophical Transactions of the Royal Society of London. Series A: Mathematical, Physical and Engineering Sciences 359 (1778) (2001) 61–96. doi:10.1098/rsta.2000.0714.

[49] D. S. Whitehead, Effect of mistuning on the vibration of turbo-machine blades induced by wakes, Journal of mechanical engineering science 8 (1) (1966) 15–21.

[50] D. S. Whitehead, The Maximum Factor by Which Forced Vibration of Blades Can Increase Due to Mistuning, Journal of Engineering for Gas Turbines and Power 120 (1) (1998) 115–119. doi:10.1115/1.2818061.

[51] B. Xiao, A. J. Rivas-Guerra, M. P. Mignolet, Maximum amplification of blade response due to mistuning in multi-degree-of-freedom blade models, in: Turbo Expo: Power for Land, Sea, and Air, Vol. 41715, 2004, pp. 427–438. doi:10.1115/gt2004-54030.

[52] J. A. Kenyon, J. H. Griffin, N. E. Kim, Sensitivity of Tuned Bladed Disk Response to Frequency Veering, Journal of Engineering for Gas Turbines and Power 127 (4) (2004) 835–842. doi:10.1115/1.1924486.

[53] D. Hemberger, D. Filsinger, H.-J. Bauer, Investigations on maximum amplitude amplification factor of real mistuned bladed structures, in: Turbo Expo: Power for Land, Sea, and Air, Vol. 44731, American Society of Mechanical Engineers, 2012, pp. 1041–1052. doi:10.1115/gt2012-68084.

[54] L. Schwerdt, S. Willeke, L. P.-v. Scheidt, J. Wallaschek, Reduced-order modeling of bladed disks considering small mistuning of the disk sectors, Journal of Engineering for Gas Turbines and Power 141 (5) (2019). doi:10.1115/1.4041071.

[55] A. Sinha, Reduced-order model of a bladed rotor with geometric mistuning, Journal of Turbomachinery 131 (3) (2009). doi:10.1115/1.2987237.

[56] M. Mbaye, C. Soize, J.-P. Ousty, A reduced-order model of detuned cyclic dynamical systems with geometric modifications using a basis of cyclic modes, Journal of engineering for gas turbines and power 132 (11) (2010). doi:10.1115/1.4000805.

[57] A. Madden, B. I. Epureanu, S. Filippi, Reduced-order modeling approach for blisks with large mass, stiffness, and geometric mistuning, AIAA journal 50 (2) (2012) 366–374. doi:10.2514/1.j051140.

[58] W. Tang, B. I. Epureanu, S. Filippi, Models for blisks with large blends and small mistuning, Mechanical Systems and Signal Processing 87 (2017) 161–179. doi:10.1016/j.ymssp.2016.10.019.

[59] L. Schwerdt, L. Panning-von Scheidt, J. Wallaschek, A Model Reduction Method for Bladed Disks With Large Geometric Mistuning Using a Partially Reduced Intermediate System Model, Journal of Engineering for Gas Turbines and Power (2020). doi:10.1115/gt2020-14199.

[60] C. Joannin, B. Chouvion, F. Thouverez, J.-P. Ousty, M. Mbaye, A nonlinear component mode synthesis method for the computation of steady-state vibrations in non-conservative systems, Mechanical Systems and Signal Processing 83 (2017) 75–92. doi:10.1016/j.ymssp.2016.05.044.

[61] S. Quaegebeur, B. Chouvion, F. Thouverez, Nonlinear cyclic reduction for the analysis of mistuned cyclic systems, Journal of Sound and Vibration 499 (2021) 116002. doi:10.1016/j.jsv.2021.116002.

[62] D. J. Morton, J. M. Tyler, J. R. Dorroh, A new 3d finite element for adaptive h-refinement in 1-irregular meshes, International journal for numerical methods in engineering 38 (23) (1995) 3989–4008.

Graphical Abstract

Modelling and analysis of a bladed drum subject to the Coriolis and mistuning effects

Anthony Tacher, Fabrice Thouverez, Jason Armand

Bladed drum model

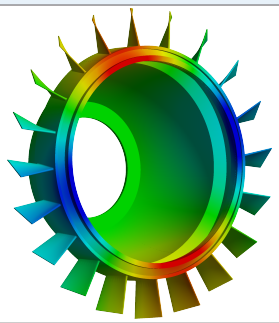

Different regions of study

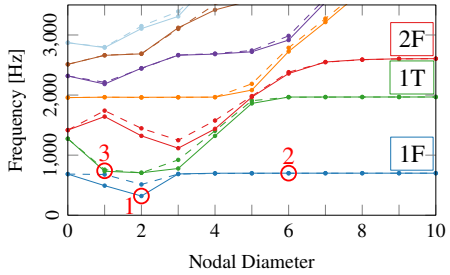

Monte Carlo analysis & results

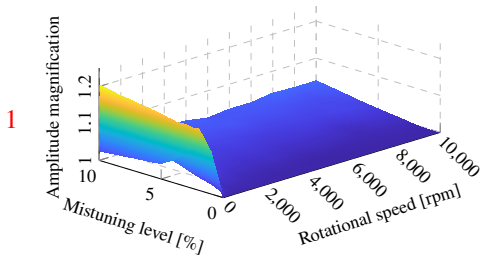

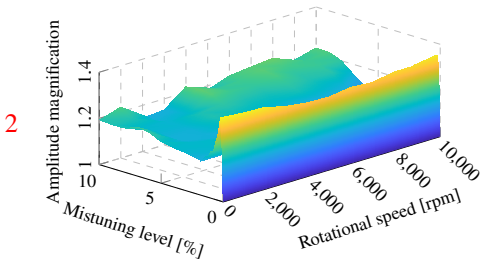

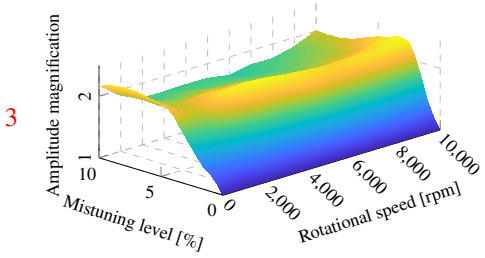

Validation of reduction techniques for mistuning and Coriolis effects

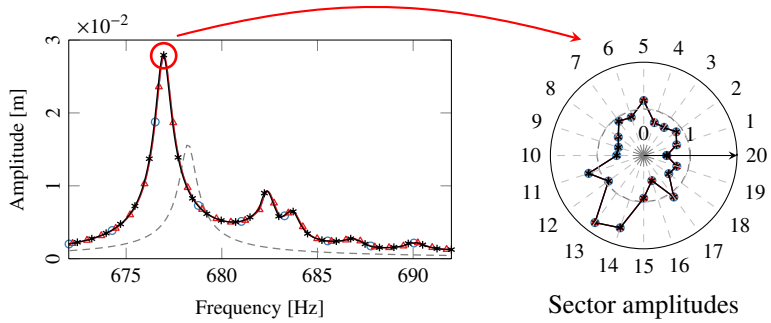

[—⊖—] SNM ROM [—△—] CMM ROM

[—✱—] Mistuned FEM [- - -] Tuned FEM